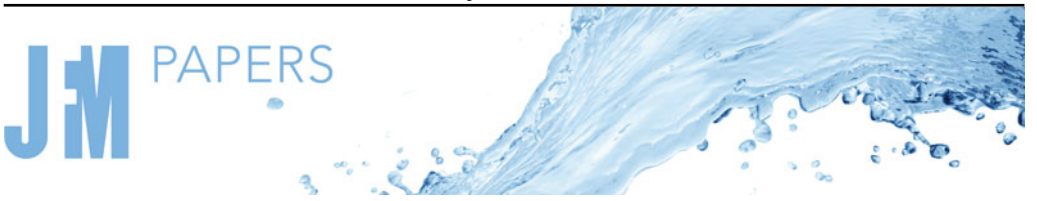
J. Fluid Mech. (2025), *vol.* 1020, A54, doi:10.1017/jfm.2025.10691



Multi-scale method for the solution of the concentration distribution in a two-layered channel flow

Anupama Bairagi[1] **and Subhendu Bikash Hazra**[1]

[1]Department of Mathematics, Bankura University, Bankura 722155, West Bengal, India

Corresponding author: Anupama Bairagi, anupama.math.bku23@gmail.com

(Received 4 July 2024; revised 30 August 2025; accepted 4 September 2025)

In this work the fascinating dynamics of a two-layered channel flow characterised by the dispersion in composite media within its layers is investigated in depth. The top layer comprises of a fluid zone that allows the fluid to travel along its surface easily (with relatively higher velocity), while the bottom layer is packed with porous media. The primary objective of this research is to do an in-depth investigation of the complex two-dimensional concentration distribution of a passive solute discharged from the inflow region. A multi-scale perturbation analysis approach has been implemented to address the system's inherent complexity. This accurate determination of the dispersion coefficient, mean concentration distribution and two-dimensional concentration distribution is accomplished deftly using Mei's homogenisation approach up to second-order approximation, which satisfactorily capture the minor variations in the solute dynamics also. The influence of various flow and porous media elements on these basic parameters is thoroughly investigated, expanding our comprehension of the complex interaction between flow dynamics and porous media's properties. The effect of Darcy number and the ratio of two viscosities (M) on the dispersion coefficient depends on the height of the porous layer. As the Péclet number ratio increases, the dispersion coefficient experiences a concurrent increase, resulting in a decline in the concentration peak. The results of the analytical studies have also been compared with those results obtained using a purely computational method to establish the validity of our studies. Both the sets of results show quite good agreement with each other. In this study, alternate flow models have been used for the porous region, and the outcomes are compared to determine which approach yields more suitable results under different conditions.

Key words: Taylor-Couette flow, porous media, dispersion

© The Author(s), 2025. Published by Cambridge University Press.

https://doi.org/10.1017/jfm.2025.10691 Published online by Cambridge University Press

1. Introduction

Studying the dispersion of solute transport in fluid and porous media is a crucial aspect of applied science and engineering. This process plays a vital role, among others, in effectively extracting crude oil from petroleum reservoir rocks, evaluating environmental risks and treating groundwater. Another area of interest is the spreading of aerosols, which are tiny dust particles floating in the air that can cause harm to human health. Dispersion through porous media is particularly relevant in addressing various challenges, including radioactive and reclaimed sewage disposal into aquifers, fertiliser movement in soil/groundwater, blood flow through capillaries, micro-fluidic systems, biomedical flows and lab-on-a-chip devices. Through the analysis of solute transport, we can gain insights into the complex mechanisms that occur at the micro-scale level, including diffusion, advection and dispersion. In fluids, dispersion refers to the spreading of a substance (such as solute, particle or contaminant) through a combination of fluid movement and molecular diffusion. Diffusion is the process by which particles (such as molecules or atoms) move from an area of higher concentration to the lower concentration, driven by their random motion. This movement continues until the particles are evenly distributed throughout the space, resulting in an equilibrium. Knowledge and understanding of these processes are essential for ensuring the safe and efficient use of natural resources and protecting the environment, as well as human health.

The work of Taylor (1953) explored the release of passive solutes in narrow tubes, revealing that solute dispersion (named Taylor dispersion) is influenced by molecular diffusivity and non-uniform solvent velocity. Taylor's model, expressing the diffusion coefficient, has been widely useful over time. Building upon Taylor's findings, Aris (1956, 1960) extended the analysis, introducing the concentration moment method to study solute distribution growth rate variance. They demonstrated that this variance equals the sum of Taylor and molecular diffusion coefficients. Researchers Gill & Sankarasubramanian (1970), Gill, Sankarasubramanian & Taylor (1971) and Sankarasubramanian & Gill (1972) advanced the study of solute dispersion in fully developed, uniform and laminar flows, offering a novel approach for understanding solute behaviour in time-varying conditions. Fischer (1973) explored longitudinal dispersion and turbulence mixing in open channels, while Mazumder & Das (1992) investigated the impact of first-order heterogeneous reactions on dispersion in pulsating flows, noting deviations from Gaussianity due to boundary absorption effects. Hazra *et al.* (1996, 1997) discussed solute dispersion in oscillatory flows of viscoelastic fluids, considering parameters like amplitude and pulsation frequency. Ault, Shin & Stone (2018) explored how particles move in narrow channels due to solute concentration gradients, focusing on diffusiophoresis and diffusioosmosis. The study develops models to control particle behaviour, with applications in particle sorting, particle concentrating and microfluidic zeta potentiometry. Shin *et al.* (2016) investigated solute gradient enhanced colloidal transport in dead-end channels, with larger particles concentrating more deeply due to size-dependent diffusiophoresis, useful for particle sorting and targeted drug delivery. Hinton & Woods (2019) explored the depth-dependent permeability affects on tracer movement in a horizontal aquifer and showed that permeability gradients cause varying flow patterns, influencing how tracers disperse; such findings are important for understanding tracer behaviour in applications like CO_2 storage. Sahu & Neufeld (2020) examined dispersion causing fluid mixing in porous media, increasing the current's volume over time; this study combines theory and experiments with implications for CO_2 sequestration and groundwater flow.

Hydrodynamic dispersion happens in porous media, combining the molecular diffusion with variation in flow velocity through interconnected pores. The works of dispersion in porous media literature have been carried out mainly in a single-zone model. However,

https://doi.org/10.1017/jfm.2025.10691 Published online by Cambridge University Press

it occurs as a double or multilayered zone in real situations such as wetland flows, nuclear contaminant transport, etc. In their theoretical analysis, Bear (1961) explored anisotropic solute dispersion in porous media, emphasising the impact of flow directions and anisotropic properties. Brezinski & Buffone (1966) conducted experiments on solute dispersion in packed beds, revealing insights into how bed characteristics influence dispersion behaviour in industrial processes. Meanwhile, Millington (1967) contributed a comprehensive theoretical analysis of solute dispersion in porous media, considering factors like flow velocity, diffusion coefficient and porous media properties. Bear (2013)'s book on solute transport in porous media covers dispersion with theoretical frameworks, mathematical models and empirical research. Cvetkovic, Dagan & Cheng (1998) extensively examined solute transport in geological formations with varying hydraulic conductivity, emphasising the effects of heterogeneity on dispersion. Cvetkovic & Dagan (1994) investigated scale effects on solute dispersion in heterogeneous porous formations, quantitatively exploring the influence of varying degrees of heterogeneity on solute transport behaviour. Nield *et al.* (2006) comprehensively covered convection in porous media, incorporating theoretical models, numerical methods and practical applications.

Beavers & Joseph (1967) contributed to fluid dynamics by investigating fluid flow in a composite region and using Darcy's law to model the flow in porous regions. Poulikakos & Kazmierczak (1987) conducted a study on forced convection in a partially filled duct with porous material. Kuznetsov (1996, 1998) employed analytical methods to investigate fluid flow in a composite region partially filled with porous media and clear fluid. Alazmi & Vafai (2001) explored fluid layer–porous medium interaction, considering factors such as porosity, interfacial resistance and convective heat transfer.

Minimal literature is available regarding the dispersion of solute transport in the composite region. Chen & Wu (2012) investigated scalar dispersion in two zone-packed regions within a tube with non-uniform flow velocity, highlighting the impact of heterogeneity on dispersion. Kumar *et al.* (2012) investigated an analytical solution for solute dispersion between two parallel plates containing porous and fluid regions, showing a decreased dispersion coefficient with higher porous parameters.

Mei, Auriault & Ng (1996) introduced a multi-scale method for finding solute dispersion in single-phase fluid flows. Wu & Chen (2014), Wang *et al.* (2019), Barik & Dalal (2019), Poddar *et al.* (2021), Das *et al.* (2021), Dhar *et al.* (2021) used the multi-scale method to solve concentration distribution for different geometries.

No work has been found using the multi-scale method for finding solute dispersion in a two-layered channel flow. Our study introduces several novel contributions to the field of fluid flow and solute dispersion in the composite media. We extend Taylor's classical dispersion theory, which is typically applied to single-phase flow in homogeneous tubes, to a dual-layered channel flow. The paper's objectives focus on analysing solute movement in a two-layered channel. These objectives include:

(i) finding the Taylor dispersivity in the channel using perturbation analysis techniques;
(ii) analysing the impact of diverse flow conditions, channel properties and additional factors on solute particle dispersion;
(iii) determining the mean concentration and two-dimensional concentration distribution of solutes in the channel, which is crucial to comprehending solute transport;
(iv) demonstrating the correlations between mean solute concentrations and various parameters, such as Darcy number, pressure gradient, height of the porous region and the Péclet numbers;
(v) validating the results of the analytical studies with those obtained by computational studies;

https://doi.org/10.1017/jfm.2025.10691 Published online by Cambridge University Press

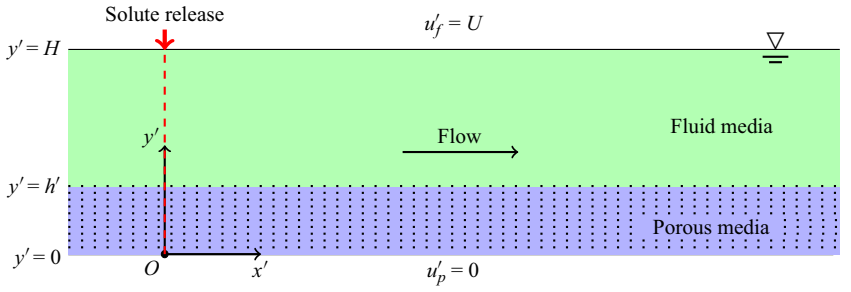


Figure 1. Sketch for the instantaneous release of solute in a two-layered channel.

(vi) analysing both the classical Darcy and extended Darcy models to determine which model is more appropriate. The multi-scale method provides an analytical solution for two-layered channel flow with multiple applications. These include understanding the dispersion and conveyance of contaminants in subsurface water-bearing geological formations, soil remediation, subsurface oil spills and the movement of pollutants in groundwater resources. A real-life application of these findings can be seen in groundwater contamination scenarios, where stratified aquifers necessitate predictions of contaminant behaviour; using our derived models, environmental engineers can assess solute dispersion, leading to improved remediation strategies to protect water quality.

2. Formulation of the problem

This study focuses on analysing a unidirectional fully developed flow within a two-layered channel possessing a distinctive configuration. The channel of width H comprises of two distinct layers: an upper layer filled with fluid having a free surface and a lower layer permeated by a porous medium with uniform permeability. In order to ensure a precise analysis of the solute transport phenomenon, specific fundamental assumptions and conditions are employed, which have been explained below.

Firstly, velocity continuity is imposed, which mandates that the fluid's velocity remains uniform throughout the interface separating the two layers. This stipulation guarantees that the fluid velocity in the lower layer, which is a porous medium, is equivalent to the fluid velocity at the free surface in the upper layer and that this equivalence occurs at their interface. Moreover, a no-slip boundary condition is enforced at the impermeable wall, typically located at the bottom of the lower layer.

Figure 1 depicts a schematic diagram of the problem. The fluid motion in the porous region is governed by the extended Darcy equation (Vafai & Kim 1990, 1995)

$$-\frac{\mathrm{d}p}{\mathrm{d}x'} + \mu_e \frac{\mathrm{d}^2 u'_p(y')}{\mathrm{d}y'^2} - \mu \frac{u'_p(y')}{\kappa} = 0, \quad 0 \leqslant y' \leqslant h', \tag{2.1}$$

and the fluid motion in the fluid region is governed by the Stokes equation (Kuznetsov 1998)

$$-\frac{\mathrm{d}p}{\mathrm{d}x'} + \mu \frac{\mathrm{d}^2 u'_f(y')}{\mathrm{d}y'^2} = 0, \quad h' \leqslant y' \leqslant H, \tag{2.2}$$

where $u'_p(y')$ and $u'_f(y')$ are fluid velocities in the porous region and fluid region, respectively, κ is the permeability of the porous medium and h' is the thickness or depth of the porous layer; μ is the fluid viscosity and μ_e is the effective viscosity representing

https://doi.org/10.1017/jfm.2025.10691 Published online by Cambridge University Press

an apparent viscosity that includes the resistance effects from porous media or complex flow conditions. It varies based on factors like porosity and permeability and is generally higher than dynamic viscosity, which is the inherent resistance of a pure fluid to flow. Both share the same units, but effective viscosity adjusts for environmental factors, making it a variable property (Givler & Altobelli 1994, Martys, Bentz & Garboczi 1994). The pressure gradient $(-\mathrm{d}p/\mathrm{d}x')$ in (2.1) and (2.2) is constant and equal (Ochoa-Tapia & Whitaker 1995). We mention that the use of (2.1) is sometimes questionable, however, in a recent study, Winter *et al.* (2022) showed that when the fluid from the high velocity flow region infiltrates into the porous region, the inertia effects dominate. In such cases, the Darcy-extended model would better predict results than the use of the pure Darcy model.

Consider the transport of a scalar quantity in a fully developed, unidirectional flow through a dual-layered channel, where the channel's length is much larger than its depth, in a Cartesian coordinate system with the longitudinal x' axis aligned with the flow direction, the y' axis aligned with the lateral direction and the origin set at one of the channel bank walls, as shown in figure 1.

The problem of solute transport in a porous region and a fluid region can be respectively formulated as (Mei & Vernescu 2010)

$$\frac{\partial C_p'}{\partial t'} + u_p'(y')\frac{\partial C_p'}{\partial x'} = D_p\left(\frac{\partial^2 C_p'}{\partial x'^2} + \frac{\partial^2 C_p'}{\partial y'^2}\right), \quad 0 < y' \leqslant h', \tag{2.3}$$

$$\frac{\partial C_f'}{\partial t'} + u_f'(y')\frac{\partial C_f'}{\partial x'} = D_f\left(\frac{\partial^2 C_f'}{\partial x'^2} + \frac{\partial^2 C_f'}{\partial y'^2}\right), \quad h' \leqslant y' < H, \tag{2.4}$$

where D_p and D_f are the diffusion coefficients in the porous region and fluid region, respectively, assumed to be constants, t' is the time, and $C_p(x', y', t')$ and $C_f'(x', y', t')$ are the concentrations of the diffusive substance in the porous region and fluid region, respectively.

2.1. *Initial and boundary conditions*

The no-slip condition is applied at the bottom of the channel, i.e.

$$u_p'(y') = 0 \quad \text{at } y' = 0. \tag{2.5}$$

The continuity of the average velocity and continuity of stress jump conditions are applied at the interface as

$$u_p'(y') = u_f'(y') \quad \text{at } y' = h', \tag{2.6}$$

and

$$\mu_e \frac{\mathrm{d}u_p'(y')}{\mathrm{d}y'} = \mu \frac{\mathrm{d}u_f'(y')}{\mathrm{d}y'} \quad \text{at } y' = h'. \tag{2.7}$$

Here U is the flow velocity of the free surface, i.e.

$$u_f'(y') = U \quad \text{at } y' = H. \tag{2.8}$$

The initial conditions for the solute transport equations are

$$C_p'(x', y', t')\,|_{t'=0} = \frac{Q_m \delta\left(\dfrac{x'}{H}\right)}{H}, \quad 0 < y' \leqslant h', \tag{2.9}$$

https://doi.org/10.1017/jfm.2025.10691 Published online by Cambridge University Press

$$C_f'(x', y', t')\,|_{t'=0} = \frac{Q_m \delta\left(\dfrac{x'}{H}\right)}{H}, \quad h' \leqslant y' < H, \tag{2.10}$$

where Q_m is the released mass at $t' = 0$ and $\delta(\cdot)$ is the Dirac delta function.

The boundary conditions for solute transport are given as

$$\left.\frac{\partial C_p'}{\partial y'}\right|_{y'=0} = \left.\frac{\partial C_f'}{\partial y'}\right|_{y'=H} = 0, \tag{2.11}$$

and the symmetry condition is applied as

$$C_p'\,|_{y'=h'} = C_f'\,|_{y'=h'}, \tag{2.12}$$

and

$$D_p \left.\frac{\partial C_p'}{\partial y'}\right|_{y'=h'} = D_f \left.\frac{\partial C_f'}{\partial y'}\right|_{y'=h'}. \tag{2.13}$$

At significant distances the tracer concentrations are considered negligible, i.e.

$$C_p'(x', y', t')\,|_{x'\to\pm\infty} = 0, \quad 0 < y' \leqslant h', \tag{2.14}$$

$$C_f'(x', y', t')\,|_{x'\to\pm\infty} = 0, \quad h' \leqslant y' < H. \tag{2.15}$$

3. Theoretical model

3.1. *Dimensionless governing equations*

The following dimensionless variables are introduced to make governing equations dimensionless:

$$x = \frac{x'}{L}, \quad y = \frac{y'}{H}, \quad h = \frac{h'}{H}, \quad C = \frac{C'}{Q_m/H}, \quad t = \frac{t'}{L/U}, \quad u_p = \frac{u_p'}{U}, \quad u_f = \frac{u_f'}{U},$$
$$Pe_p = \frac{UH}{D_p}, \quad Pe_f = \frac{UH}{D_f}, \; D_a = \frac{\kappa}{H^2}, \quad Q = -\frac{\mathrm{d}p}{\mathrm{d}x'} \Big/ \frac{\mu U}{H^2}, \quad M = \frac{\mu_e}{\mu}. \tag{3.1}$$

The angle bracket denotes the section average defined as

$$\langle u \rangle = \int_0^h u_p(y)\mathrm{d}y + \int_h^1 u_f(y)\mathrm{d}y. \tag{3.2}$$

Using the dimensionless variables, we get the velocity profiles after solving (2.1) and (2.2), together with initial conditions and boundary conditions (2.5)–(2.8) as follows:

$$u_p(y) = QD_a\left(1 - \cosh\left\{\frac{y}{\sqrt{MD_a}}\right\}\right) + d_2 \sinh\left\{\frac{y}{\sqrt{MD_a}}\right\} \tag{3.3}$$

and

$$u_f(y) = 1 - d_1(1 - y) + \frac{Q}{2}\left(1 - y^2\right). \tag{3.4}$$

https://doi.org/10.1017/jfm.2025.10691 Published online by Cambridge University Press

Here d_1 and d_2 are given as

$$d_1 = d_2\sqrt{\frac{M}{D_a}}\cosh\left\{\frac{1}{\sqrt{MD_a}}h\right\} - Q\sqrt{MD_a}\sinh\left\{\frac{1}{\sqrt{MD_a}}h\right\} + hQ, \tag{3.5}$$

$$d_2 = \frac{1+\frac{1}{2}Q(1-h)^2 - QD_a\left(1-\cosh\left\{\frac{1}{\sqrt{MD_a}}h\right\}\right) + (1-h)Q\sqrt{MD_a}\sinh\left\{\frac{1}{\sqrt{MD_a}}h\right\}}{\sinh\left\{\frac{1}{\sqrt{MD_a}}h\right\} + \sqrt{\frac{M}{D_a}}(1-h)\cosh\left\{\frac{1}{\sqrt{MD_a}}h\right\}}. \tag{3.6}$$

The dimensionless form of governing equations and initial and boundary conditions for solute transport in the porous region and the fluid region will be reduced to, respectively,

$$\epsilon\frac{\partial C_p}{\partial t} + \epsilon u_p\frac{\partial C_p}{\partial x} = \frac{1}{Pe_p}\left(\epsilon^2\frac{\partial^2 C_p}{\partial x^2} + \frac{\partial^2 C_p}{\partial y^2}\right), \quad 0 < y \leqslant h, \tag{3.7}$$

$$\epsilon\frac{\partial C_f}{\partial t} + \epsilon u_f\frac{\partial C_f}{\partial x} = \frac{1}{Pe_f}\left(\epsilon^2\frac{\partial^2 C_f}{\partial x^2} + \frac{\partial^2 C_f}{\partial y^2}\right), \quad h \leqslant y < 1, \tag{3.8}$$

$$C_p(x, y, t)\,|_{t=0} = \delta\left(\frac{x}{\epsilon}\right), \quad 0 < y \leqslant h, \tag{3.9}$$

$$C_f(x, y, t)\,|_{t=0} = \delta\left(\frac{x}{\epsilon}\right), \quad \leqslant h < y < 1, \tag{3.10}$$

$$\left.\frac{\partial C_p}{\partial y}\right|_{y=0} = \left.\frac{\partial C_f}{\partial y}\right|_{y=1} = 0, \tag{3.11}$$

$$C_p\,|_{y=h} = C_f\,|_{y=h}, \tag{3.12}$$

$$\left.\frac{1}{Pe_p}\frac{\partial C_p}{\partial y}\right|_{y=h} = \left.\frac{1}{Pe_f}\frac{\partial C_f}{\partial y}\right|_{y=h}, \tag{3.13}$$

and

$$C_p(x, y, t)\,|_{x\to\pm\infty} = 0, \quad 0 < y \leqslant h, \tag{3.14}$$

$$C_f(x, y, t)\,|_{x\to\pm\infty} = 0, \quad h \leqslant y < 1. \tag{3.15}$$

3.2. *Asymptotic analysis*

The multi-scale approach is an incredibly effective methodology for tackling problems that depend on multiple scales. Employing an 'averaging out' process, it transforms complex microscopic equations into more manageable macroscopic ones especially for the porous region. This approach is beneficial for solving problems with significant differences in scale. Mei (1992), Mei *et al.* (1996) introduced homogenisation techniques in fluid dynamics, which have provided a systematic approach for studying dispersion in single-phase fluid flows and inspired several subsequent studies such as Ng & Mei (1996). When examining the process of passive solute transport in a two-layered channel flow, it is necessary to consider two distinct length scales: H, which represents the depth of the channel; and L, which represents the characteristic longitudinal length of the solute cloud. In addition, two relevant time scales must be taken into account: T_0, denoting the convection time across L, expressed as $T_0 = L/U$ (with U representing free surface velocity); and T_1, representing the diffusion time across L, expressed as $T_1 = L^2/D$ (here,

https://doi.org/10.1017/jfm.2025.10691 Published online by Cambridge University Press

$D = D_p$ in the porous region and $D = D_f$ in the fluid region). Their ratio is $T_0 : T_1 = 1 : 1/\epsilon$, where $\epsilon\ (= H/L \ll 1)$ is the perturbation parameter that represents the relationship between the channel depth H and the characteristic length L. In this analysis we have considered that $O(Pe_p) = O(Pe_f) = 1$. Based on the time scales, two-time variables, $t_0 = t$ and $t_1 = \epsilon t$, are introduced to effectively analyse the system's dynamics at different scales. This approach helps us to better understand the transport phenomena and allows us to create simplified macroscopic equations that are easier to analyse and solve.

The time derivative is expanded using the chain rule as (Chen & Wu 2012)

$$\frac{\partial}{\partial t} = \frac{\partial}{\partial t_0} + \epsilon \frac{\partial}{\partial t_1}. \tag{3.16}$$

In multi-scale approaches the concentrations C_p and C_f are expanded as (Chen & Wu 2012)

$$C_p(x, y, t) = C_p^{(0)}(x, y, t_0, t_1) + \epsilon C_p^{(1)}(x, y, t_0, t_1) + \epsilon^2 C_p^{(2)}(x, y, t_0, t_1) + \ldots + O(\epsilon^n) \tag{3.17}$$

and

$$C_f(x, y, t) = C_f^{(0)}(x, y, t_0, t_1) + \epsilon C_f^{(1)}(x, y, t_0, t_1) + \epsilon^2 C_f^{(2)}(x, y, t_0, t_1) + \ldots + O(\epsilon^n). \tag{3.18}$$

Substituting (3.16)–(3.18) into (3.7)–(3.13), the $O(\epsilon^0)$ approximation is obtained as

$$\frac{\partial^2 C_p^{(0)}}{\partial y^2} = 0, \quad 0 < y \leqslant h, \tag{3.19}$$

$$\frac{\partial^2 C_f^{(0)}}{\partial y^2} = 0, \quad h \leqslant y < 1, \tag{3.20}$$

$$\left.\frac{\partial C_p^{(0)}}{\partial y}\right|_{y=0} = \left.\frac{\partial C_f^{(0)}}{\partial y}\right|_{y=1} = 0, \tag{3.21}$$

$$C_p^{(0)}\,|_{y=h} = C_f^{(0)}\,|_{y=h}, \tag{3.22}$$

$$\left.\frac{1}{Pe_p}\frac{\partial C_p^{(0)}}{\partial y}\right|_{y=h} = \left.\frac{1}{Pe_f}\frac{\partial C_f^{(0)}}{\partial y}\right|_{y=h}. \tag{3.23}$$

We can conclude that from (3.19)–(3.23),

$$C^{(0)}(x, t_0, t_1) = \begin{cases} C_p^{(0)}(x, t_0, t_1), & 0 < y \leqslant h, \\ C_f^{(0)}(x, t_0, t_1), & h \leqslant y < 1. \end{cases} \tag{3.24}$$

Substituting (3.16)–(3.18) into (3.7)–(3.13), the $O(\epsilon)$ approximation is obtained as

$$\frac{\partial C_p^{(0)}}{\partial t_0} + u_p(y)\frac{\partial C_p^{(0)}}{\partial x} = \frac{1}{Pe_p}\frac{\partial^2 C_p^{(1)}}{\partial y^2}, \quad 0 < y \leqslant h, \tag{3.25}$$

$$\frac{\partial C_f^{(0)}}{\partial t_0} + u_f(y)\frac{\partial C_f^{(0)}}{\partial x} = \frac{1}{Pe_f}\frac{\partial^2 C_f^{(1)}}{\partial y^2}, \quad h \leqslant y < 1, \tag{3.26}$$

$$\left.\frac{\partial C_p^{(1)}}{\partial y}\right|_{y=0} = \left.\frac{\partial C_f^{(1)}}{\partial y}\right|_{y=1} = 0, \tag{3.27}$$

https://doi.org/10.1017/jfm.2025.10691 Published online by Cambridge University Press

$$C_p^{(1)}\,|_{y=h} = C_f^{(1)}\,|_{y=h}, \tag{3.28}$$

$$\frac{1}{Pe_p}\frac{\partial C_p^{(1)}}{\partial y}\bigg|_{y=h} = \frac{1}{Pe_f}\frac{\partial C_f^{(1)}}{\partial y}\bigg|_{y=h}. \tag{3.29}$$

We apply the section average with respect to the spatial variable y of (3.25) and (3.26) to obtain

$$\frac{\partial C^{(0)}}{\partial t_0} + \langle u\rangle \frac{\partial C^{(0)}}{\partial x} = 0. \tag{3.30}$$

Subtracting (3.30) from (3.25) and (3.26) and using the relationship (3.24), we have

$$\frac{\partial^2 C_p^{(1)}}{\partial y^2} = Pe_p(u_p - \langle u\rangle)\frac{\partial C^{(0)}}{\partial x}, \quad 0 < y \leqslant h, \tag{3.31}$$

and

$$\frac{\partial^2 C_f^{(1)}}{\partial y^2} = Pe_f(u_f - \langle u\rangle)\frac{\partial C^{(0)}}{\partial x}, \quad h \leqslant y < 1. \tag{3.32}$$

Since advection in the y direction is negligible, this assumption allows the system to exhibit separability in x and y:

$$C_p^{(1)} = Pe_p N_p(y)\frac{\partial C^{(0)}}{\partial x}, \quad 0 < y \leqslant h, \tag{3.33}$$

$$C_f^{(1)} = Pe_f N_f(y)\frac{\partial C^{(0)}}{\partial x}, \quad h \leqslant y < 1. \tag{3.34}$$

Here the transverse functions $N_p(y)$ and $N_f(y)$ can be respectively found from the equations

$$\frac{\mathrm{d}^2 N_p(y)}{\mathrm{d}y^2} = u_p(y) - \langle u\rangle, \quad 0 < y \leqslant h, \tag{3.35}$$

$$\frac{\mathrm{d}^2 N_f(y)}{\mathrm{d}y^2} = u_f(y) - \langle u\rangle, \quad h \leqslant y < 1, \tag{3.36}$$

with the boundary conditions

$$\frac{\partial N_p}{\partial y}\,|_{y=0} = \frac{\partial N_f}{\partial y}\,|_{y=1} = 0, \tag{3.37}$$

$$Pe_p N_p(y)\,|_{y=h} = Pe_f N_f(y)\,|_{y=h}, \tag{3.38}$$

$$\frac{\partial N_p}{\partial y}\,|_{y=h} = \frac{\partial N_f}{\partial y}\,|_{y=h}, \tag{3.39}$$

and the consistency condition

$$\langle PeN\rangle = Pe_p\int_0^h N_p(y)\mathrm{d}y + Pe_f\int_h^1 N_f(y)\mathrm{d}y = 0. \tag{3.40}$$

https://doi.org/10.1017/jfm.2025.10691 Published online by Cambridge University Press

After solving (3.35) and (3.36), we get

$$N_p(y) = QD_a\left\{\frac{y^2}{2} - MD_a\cosh\left(\frac{y}{\sqrt{MD_a}}\right)\right\} + d_2\left\{MD_a\sinh\left(\frac{y}{\sqrt{MD_a}}\right) - \sqrt{MD_a}\,y\right\} - \langle u\rangle\frac{y^2}{2} + d_3 \tag{3.41}$$

and

$$N_f(y) = \left(\langle u\rangle - \frac{Q}{3} + \frac{d_1}{2} - 1\right)y + \left(\tfrac{1}{2} - \frac{d_1}{2} + \frac{Q}{4} - \frac{\langle u\rangle}{2}\right)y^2 + \frac{d_1}{6}y^3 - \frac{Q}{24}y^4 + d_4, \tag{3.42}$$

where d_3 and d_4 are given in Appendix A and $\langle u\rangle$ can be found as

$$\langle u\rangle = QD_a\left\{h - \sqrt{MD_a}\sinh\left(\frac{h}{\sqrt{MD_a}}\right)\right\} - d_2\sqrt{MD_a}\left\{1 - \cosh\left(\frac{h}{\sqrt{MD_a}}\right)\right\} + (1-h) - \frac{d_1}{2}(1-h)^2 + \frac{Q}{6}\left(2 - 3h + h^3\right), \tag{3.43}$$

where d_1 and d_2 are provided in (3.5) and (3.6), respectively.

Similarly, for $O(\epsilon^2)$ approximations, we obtain

$$\frac{\partial C_p^{(1)}}{\partial t_0} + \frac{\partial C_p^{(0)}}{\partial t_1} + u_p\frac{\partial C_p^{(1)}}{\partial x} = \frac{1}{Pe_p}\left(\frac{\partial^2 C_p^{(0)}}{\partial x^2} + \frac{\partial^2 C_p^{(2)}}{\partial y^2}\right), \tag{3.44}$$

$$\frac{\partial C_f^{(1)}}{\partial t_0} + \frac{\partial C_f^{(0)}}{\partial t_1} + u_f\frac{\partial C_f^{(1)}}{\partial x} = \frac{1}{Pe_f}\left(\frac{\partial^2 C_f^{(0)}}{\partial x^2} + \frac{\partial^2 C_f^{(2)}}{\partial y^2}\right), \tag{3.45}$$

$$\left.\frac{\partial C_p^{(2)}}{\partial y}\right|_{y=0} = \left.\frac{\partial C_f^{(2)}}{\partial y}\right|_{y=1} = 0, \tag{3.46}$$

$$C_p^{(2)}|_{y=h} = C_f^{(2)}|_{y=h}, \tag{3.47}$$

$$\left.\frac{1}{Pe_p}\frac{\partial C_p^{(2)}}{\partial y}\right|_{y=h} = \left.\frac{1}{Pe_f}\frac{\partial C_f^{(2)}}{\partial y}\right|_{y=h}. \tag{3.48}$$

Substituting (3.33) and (3.34) into (3.44) and (3.45) with the help of (3.30), we get

$$\frac{\partial C^{(0)}}{\partial t_1} = \left\{\frac{1}{Pe_p} - (u_p - \langle u\rangle)Pe_p N_p(y)\right\}\frac{\partial^2 C^{(0)}}{\partial x^2} + \frac{1}{Pe_p}\frac{\partial^2 C_p^{(2)}}{\partial y^2}, \quad 0 < y \leqslant h, \tag{3.49}$$

$$\frac{\partial C^{(0)}}{\partial t_1} = \left\{\frac{1}{Pe_f} - (u_f - \langle u\rangle)Pe_f N_f(y)\right\}\frac{\partial^2 C^{(0)}}{\partial x^2} + \frac{1}{Pe_f}\frac{\partial^2 C_f^{(2)}}{\partial y^2}, \quad h \leqslant y < 1. \tag{3.50}$$

https://doi.org/10.1017/jfm.2025.10691 Published online by Cambridge University Press

Using the averaging operation of (3.49) and (3.50), we have

$$\frac{\partial C^{(0)}}{\partial t_1} = \left[\int_0^h \left\{ \frac{1}{Pe_p} - Pe_p \left(u_p - \langle u \rangle\right) N_p(y) \right\} \mathrm{d}y + \int_h^1 \left\{ \frac{1}{Pe_f} - Pe_f \left(u_f - \langle u \rangle\right) N_f(y) \right\} \mathrm{d}y \right] \frac{\partial^2 C^{(0)}}{\partial x^2}, \tag{3.51}$$

$$\frac{\partial C^{(0)}}{\partial t_1} = \left\langle \frac{1}{Pe} - PeuN(y) \right\rangle \frac{\partial^2 C^{(0)}}{\partial x^2}, \tag{3.52}$$

where

$$\left\langle \frac{1}{Pe} - Pe\, u\, N(y) \right\rangle = \int_0^h \left\{ \frac{1}{Pe_p} - Pe_p \left(u_p - \langle u \rangle\right) N_p(y) \right\} \mathrm{d}y + \int_h^1 \left\{ \frac{1}{Pe_f} - Pe_f \left(u_f - \langle u \rangle\right) N_f(y) \right\} \mathrm{d}y. \tag{3.53}$$

Multiplying (3.52) by ϵ and adding (3.30), we have

$$\frac{\partial C^{(0)}}{\partial t_0} + \epsilon \frac{\partial C^{(0)}}{\partial t_1} + \langle u \rangle \frac{\partial C^{(0)}}{\partial x} = \epsilon \left\langle \frac{1}{Pe} - PeuN(y) \right\rangle \frac{\partial^2 C^{(0)}}{\partial x^2}. \tag{3.54}$$

Using (3.16), (3.54) becomes

$$\frac{\partial C^{(0)}}{\partial t} + \langle u \rangle \frac{\partial C^{(0)}}{\partial x} = \epsilon \left\langle \frac{1}{Pe} - PeuN(y) \right\rangle \frac{\partial^2 C^{(0)}}{\partial x^2}. \tag{3.55}$$

Using the initial and boundary conditions given in (2.9)–(2.13), the solution of (3.55) can be written in the new variables t^* and ζ, where $x = x'/L$, $t = t'/(L/U)$, $t^* = t'/(H^2/\langle D \rangle)$ and $\zeta = x'/H - \langle u \rangle t^*/\langle 1/Pe \rangle$, as

$$C^{(0)} = \frac{1}{\sqrt{4\pi D_T t^*}} \exp\left(\frac{-\zeta^2}{4 D_T t^*} \right), \tag{3.56}$$

where D_T is the effective dispersion coefficient, which is given as

$$D_T = 1 - \frac{\langle PeuN(y) \rangle}{\langle \frac{1}{Pe} \rangle}. \tag{3.57}$$

Here , the averages

$$\left\langle \frac{1}{Pe} \right\rangle = \frac{h}{Pe_p} + \frac{1-h}{Pe_f} \tag{3.58}$$

and

$$\langle Pe\, u\, N(y) \rangle = \int_0^h Pe_p \left(u_p - \langle u \rangle\right) N_p(y)\, \mathrm{d}y + \int_h^1 Pe_f \left(u_f - \langle u \rangle\right) N_f(y)\, \mathrm{d}y = Pe_p I_1 + Pe_f I_2, \tag{3.59}$$

where the parameters I_1 and I_2 are given in Appendix A.

Substituting (3.52) into (3.49) and (3.50), we get

$$\frac{1}{Pe_p} \frac{\partial^2 C_p^{(2)}}{\partial y^2} = \left[\left\langle \frac{1}{Pe} - PeuN(y) \right\rangle - \left\{ \frac{1}{Pe_p} - Pe_p (u_p - \langle u \rangle) N_p(y) \right\} \right] \frac{\partial^2 C^{(0)}}{\partial x^2} \tag{3.60}$$

https://doi.org/10.1017/jfm.2025.10691 Published online by Cambridge University Press

and

$$\frac{1}{Pe_f}\frac{\partial^2 C_f^{(2)}}{\partial y^2} = \left[\left\langle \frac{1}{Pe} - PeuN(y)\right\rangle - \left\{\frac{1}{Pe_f} - Pe_f(u_f - \langle u\rangle)N_f(y)\right\}\right]\frac{\partial^2 C^{(0)}}{\partial x^2}. \tag{3.61}$$

Since advection in the y direction is negligible, this assumption allows the system to exhibit separability. Let us consider the solutions of (3.60) and (3.61) as

$$C_p^{(2)} = Pe_p X_p(y)\frac{\partial^2 C^{(0)}}{\partial x^2}, \quad 0 < y \leqslant h, \tag{3.62}$$

and

$$C_f^{(2)} = Pe_f X_f(y)\frac{\partial^2 C^{(0)}}{\partial x^2}, \quad h \leqslant y < 1, \tag{3.63}$$

respectively, where the transverse functions $X_p(y)$ and $X_f(y)$ can be found from the equations

$$\frac{\mathrm{d}^2 X_p(y)}{\mathrm{d}y^2} = \left[\left\langle \frac{1}{Pe} - PeuN(y)\right\rangle - \left\{\frac{1}{Pe_p} - Pe_p(u_p - \langle u\rangle)N_p(y)\right\}\right] \tag{3.64}$$

and

$$\frac{\mathrm{d}^2 X_f(y)}{\mathrm{d}y^2} = \left[\left\langle \frac{1}{Pe} - PeuN(y)\right\rangle - \left\{\frac{1}{Pe_f} - Pe_f(u_f - \langle u\rangle)N_f(y)\right\}\right], \tag{3.65}$$

with the following respective boundary and uniqueness conditions:

$$\frac{\mathrm{d}X_p}{\mathrm{d}y}|_{y=0} = \frac{\mathrm{d}X_f}{\mathrm{d}y}|_{y=1} = 0, \tag{3.66}$$

$$Pe_p X_p(y)|_{y=h} = Pe_f X_f(y)|_{y=h}, \tag{3.67}$$

$$\left.\frac{\partial X_p}{\partial y}\right|_{y=h} = \left.\frac{\partial X_f}{\partial y}\right|_{y=h} \tag{3.68}$$

and

$$Pe_p\int_0^h X_p(y)\mathrm{d}y + Pe_f\int_h^1 X_f(y)\mathrm{d}y = 0. \tag{3.69}$$

Solving (3.64)–(3.69), we obtain

$$X_p(y) = \left[\left\langle \frac{1}{Pe}\right\rangle - (Pe_p I_1 + Pe_f I_2) - \frac{1}{Pe_p}\right]\frac{y^2}{2} + I_3(y) + d_9 y + d_{10}, \tag{3.70}$$

$$X_f(y) = \left[\left\langle \frac{1}{Pe}\right\rangle - (Pe_p I_1 + Pe_f I_2) - \frac{1}{Pe_f}\right]\frac{y^2}{2} + I_4(y) + d_{11} y + d_{12}, \tag{3.71}$$

where the values of the parameters I_1, I_2, d_9, d_{10}, d_{11}, d_{12} and $I_3(y)$, $I_4(y)$ are provided in Appendix A.

The solution of $O(\epsilon^0)$ is given as

$$C^{(0)} = \frac{1}{\sqrt{4\pi D_T t^*}}\exp\left(\frac{-\zeta^2}{4D_T t^*}\right). \tag{3.72}$$

https://doi.org/10.1017/jfm.2025.10691 Published online by Cambridge University Press

Parameters	Minimum	Maximum
ζ	$-\infty$	∞
y	0	1
D_a	10^{-3}	10
Pe_p	0.5	1.5
Pe_f	0.5	1.5
M	1	3
Q	0	10
t^*	1	15

Table 1. Range of parameter values.

The solutions of $O(\epsilon^1)$ are given as

$$C_p^{(1)} = Pe_p N_p(y) \frac{\partial C^{(0)}}{\partial x}, \quad 0 < y \leqslant h, \tag{3.73}$$

$$C_f^{(1)} = Pe_f N_f(y) \frac{\partial C^{(0)}}{\partial x}, \quad h \leqslant y < 1, \tag{3.74}$$

where $N_p(y)$ and $N_f(y)$ are given in (3.41) and (3.42).

The solutions of $O(\epsilon^2)$ are given as follows

$$C_p^{(2)} = Pe_p X_p(y) \frac{\partial^2 C^{(0)}}{\partial x^2}, \quad 0 < y \leqslant h, \tag{3.75}$$

and

$$C_f^{(2)} = Pe_f X_f(y) \frac{\partial^2 C^{(0)}}{\partial x^2}, \quad h \leqslant y < 1. \tag{3.76}$$

where $X_p(y)$ and $X_f(y)$ are given in (3.70) and (3.71).

4. Results and discussion

In this section we discuss the results obtained through our analysis.

4.1. *Parameter selection*

The selection of parameter values in this study is based on a comprehensive review of existing literature (Chen & Wu 2012). Table 1 presents the range of parameter values used in these investigations. The Darcy number (D_a) indicates permeability, where a higher D_a signifies more permeable, less compact pore geometry, and a lower D_a signifies less permeable, more compact geometry. The viscosity ratio (M), representing the ratio of two viscosities, is crucial for exploring the impact on fluid dynamics. The pressure gradient (Q), expressed as $-(\mathrm{d}p/\mathrm{d}x)/(\mu U/H^2)$, allows for the analysis of the influence on the composite region, with different Q values representing varying pressure gradients, facilitating the examination of flow behaviour under different pressure conditions. Finally, time (t^*) represents the temporal aspect of pollutant dispersion, enabling the analysis of how pollutant concentration and distribution evolve over time. The Péclet numbers (Pe_p and Pe_f) are dimensionless numbers that characterise the relative importance of advection to diffusion in the transport processes, with their values indicating the dominance of one mechanism over the other.

https://doi.org/10.1017/jfm.2025.10691 Published online by Cambridge University Press

4.2. *Computational results and validations*

The expression for the two-dimensional concentration distribution can be derived from (3.17) and (3.18) in the new coordinate system $\{\zeta, y\}$ as

$$C = \begin{cases} C^{(0)} + \epsilon Pe_p N_p(y)\dfrac{\partial C^{(0)}}{\partial \zeta} + \epsilon^2 Pe_p X_p(y)\dfrac{\partial^2 C^{(0)}}{\partial \zeta^2}, & 0 < y \leqslant h, \\ C^{(0)} + \epsilon Pe_f N_f(y)\dfrac{\partial C^{(0)}}{\partial \zeta} + \epsilon^2 Pe_f X_f(y)\dfrac{\partial^2 C^{(0)}}{\partial \zeta^2}, & h \leqslant y < 1. \end{cases} \tag{4.1}$$

We used the finite difference discretisation technique, as explained in Appendix D, to obtain the following discrete forms of (3.7) and (3.8) as follows:

$$\begin{aligned} &Pe_p \left\langle \frac{1}{Pe} \right\rangle \frac{C^{n+1}_{p_{i,j}} - C^{n}_{p_{i,j}}}{\Delta t^*} \\ &\quad + Pe_p \left\{ \max(u_p - \langle u \rangle, 0) \frac{C^{n}_{p_{i,j}} - C^{n}_{p_{i-1,j}}}{\Delta \zeta} - \max(\langle u \rangle - u_p, 0) \frac{C^{n}_{p_{i+1,j}} - C^{n}_{p_{i,j}}}{\Delta \zeta} \right\} \\ &= \frac{C^{n}_{p_{i+1,j}} - 2C^{n}_{p_{i,j}} + C^{n}_{p_{i-1,j}}}{\Delta \zeta^2} + \frac{C^{n}_{p_{i,j+1}} - 2C^{n}_{p_{i,j}} + C^{n}_{p_{i,j-1}}}{\Delta y^2}, \quad j = 0, 1, \ldots, j_h, \end{aligned} \tag{4.2}$$

$$\begin{aligned} &Pe_f \left\langle \frac{1}{Pe} \right\rangle \frac{C^{n+1}_{f_{i,j}} - C^{n}_{f_{i,j}}}{\Delta t^*} \\ &\quad + Pe_f \left\{ \max(u_p - \langle u \rangle, 0) \frac{C^{n}_{f_{i,j}} - C^{n}_{f_{i-1,j}}}{\Delta \zeta} - \max(\langle u \rangle - u_f, 0) \frac{C^{n}_{f_{i+1,j}} - C^{n}_{f_{i,j}}}{\Delta \zeta} \right\} \\ &= \frac{C^{n}_{f_{i+1,j}} - 2C^{n}_{f_{i,j}} + C^{n}_{f_{i-1,j}}}{\Delta \zeta^2} + \frac{C^{n}_{f_{i,j+1}} - 2C^{n}_{f_{i,j}} + C^{n}_{f_{i,j-1}}}{\Delta y^2}, \quad j = j_h, j_h + 1, \ldots N_y. \end{aligned} \tag{4.3}$$

Here $i = 0, 1, 2, \ldots, M_x$ and $j = 0, 1, 2 \ldots, N_y$; M_x and N_y represent the maximum number of grid points along the ζ and y direction, respectively. The computational domain considered is $[-20, 20] \times [0, 1]$. We discretise the domain using 2001 grid points in the longitudinal direction and 101 grid points in the transverse direction, corresponding to $\Delta x = L_x/(M_x - 1)$ and $\Delta y = L_y/(N_y - 1)$. The time step is chosen as

$$\Delta t = \frac{0.4}{(1/\Delta x^2 + 1/\Delta y^2)}, \tag{4.4}$$

which satisfies the stability condition of the explicit scheme.

In figure 2 we present a comparative analysis between the analytical and numerical results over time. The graph shows a strong relation between the two-dimensional concentration distributions obtained from both the analytical and computational approaches. Although experimental data for this specific case is not available, we have provided a comparison with results derived from computational methods. This comparison highlights the consistency between the two methods and validates the reliability of the computational model in capturing the behaviour predicted by the analytical solution. Despite the absence of experimental verification, the close agreement between these solution methods reinforces the accuracy and applicability of both methods in predicting this phenomenon.

https://doi.org/10.1017/jfm.2025.10691 Published online by Cambridge University Press

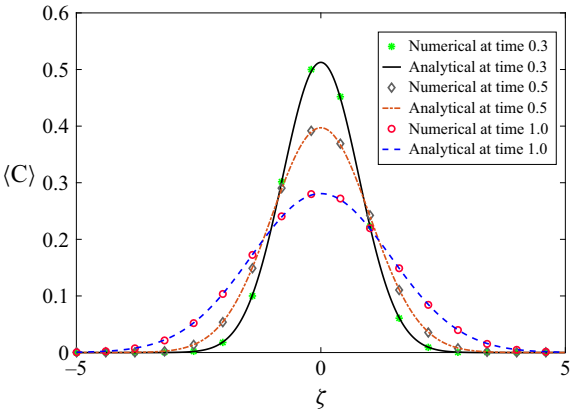


Figure 2. Comparison between analytical and numerical results of a two-dimensional concentration distribution for different times with $M = 1$, $Pe_p = Pe_f = 1$, $Q = 1$, $h = 0.5$, $D_a = 0.1$.

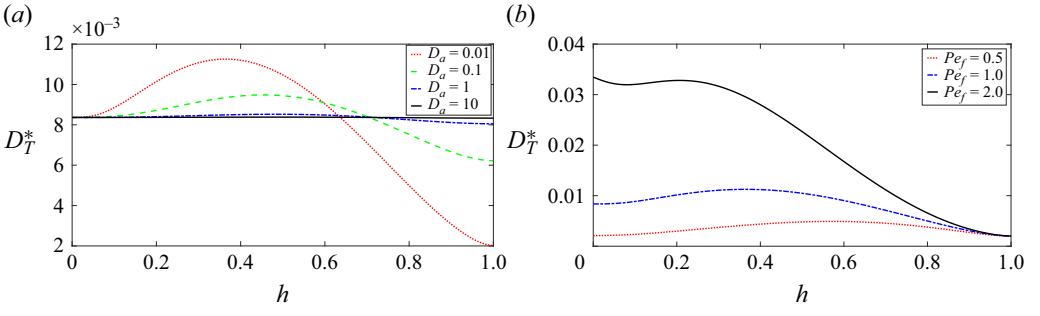


Figure 3. Variation of dispersion for (*a*) $M = 1$, $Pe_p = Pe_f = 1$, $Q = 1$ and (*b*) $D_a = 1$, $Pe_p = 1$, $M = 1$, $Q = 1$.

4.3. *Dispersion coefficients*

The effective dispersion coefficient can be expressed in (3.57) as

$$D_T = 1 + D_T^*. \tag{4.5}$$

The value of D_T^* takes into account the impact of lateral diffusion and advection and is calculated as $-\langle PeuN(y)\rangle/\langle 1/Pe\rangle$. On the right-hand side, the constant term of (4.5), i.e. the one representing the effect of longitudinal diffusion, can be safely ignored to focus on the enhanced effects of lateral diffusion and advection. The dispersion coefficient (D_T^*) is influenced by various parameters such as Pe_f, Pe_p, M, h, Q and D_a. When the Darcy number(D_a) is large, D_T^* becomes 0.0083 Pe_f^2, which is the same as the finding of Barik & Dalal (2018). This value represents the degree of dispersion of the solute in the fluid medium under single-zone open channel conditions (i.e. $h = 0$ in our case).

Figure 3(*a*) shows the variation of dispersion for different D_a values. We can see from this that an increase in D_a leads to decrease in the dispersion value and a flatter dispersion graph, which is same as in Chen & Wu (2012). When the value of D_a is 0.01, the dispersion coefficient displays a discernible pattern. It gradually increases until it reaches a specific value of h, which is not fixed for every D_a, after which it experiences a rapid decrease. When D_a is high, fluid flow through porous media becomes more efficient, and advection becomes increasingly essential compared with diffusion. When advection dominates (high D_a), the dispersion graph becomes flatter because advection rapidly homogenises the solute concentration within the porous medium. The variation of dispersion graphs with

https://doi.org/10.1017/jfm.2025.10691 Published online by Cambridge University Press

M	$h=0$	$h=0.8$	$h=1$
1.0	0.008366	0.007524	0.006224
2.0	0.008366	0.006316	0.007114
3.0	0.008366	0.0041122	0.0040339

Table 2. Values of D_T^* for different values of M and h.

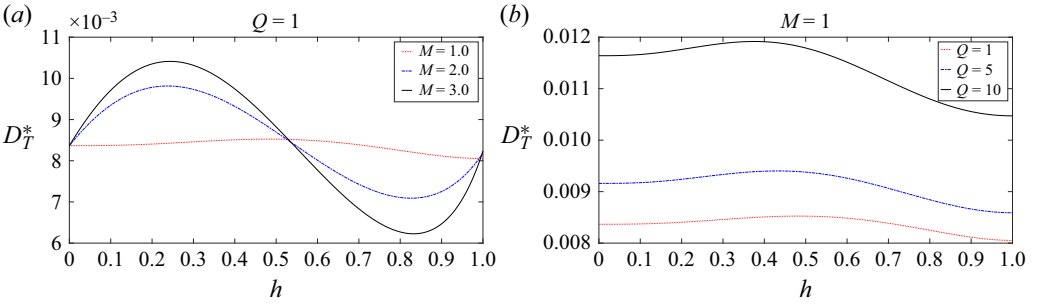


Figure 4. Variation of dispersion for (*a*) $Pe_p = Pe_f = 1$, $Q = 1$ and $D_a = 1$, and (*b*) $Pe_p = Pe_f = 1$, $M = 1$ and $D_a = 1$.

different Péclet numbers for the fluid phase (Pe_f), as depicted in figure 3(*b*), illustrates a clear relationship between Pe_f values and the dispersion coefficient. As Pe_f increases, it can be noticed that the dispersion coefficient also increases (Chen & Wu 2012).

Figure 4(*a*) illustrates the variation of dispersion coefficient with respect to the height of the porous region, h, for different values of M, which represents the ratio of effective viscosity to the dynamic viscosity. For each value of M, the dispersion initially increases as h increases from 0 to 0.3, and then shows varying behaviour for higher h. When $h = 0.5$, the dispersion remains relatively stable or slightly decreases, but for higher values of h (around 0.8 and 1), we observe a general decline in dispersion. The height of the porous region, h, affects the flow dynamics and the spread of particles within the porous medium. At lower heights ($h = 0$ to $h = 0.3$), the flow is less constrained because the porous region is not fully developed, leading to weaker interactions between the fluid and porous medium. As a result, the dispersion initially increases due to less resistance and more mobility of fluid particles. However, as h increases, the porous medium becomes more dominant, imposing greater resistance to flow, which in turn slows down the dispersion. This leads to a peak or plateau in dispersion values around $h = 0.3$, followed by a decline as the resistance further increases with larger h. This phenomenon can be seen in the values displayed in table 2.

Table 3 and figure 4(*b*) present the variations in dispersion coefficient (D_T^*) as influenced by the height (h) of the porous region and the pressure gradient (Q). With a constant pressure gradient, the dispersion coefficient increases with the increase in the height of the porous region, and with a fixed height of the porous medium, the dispersion coefficient increases as the pressure gradient increases.

4.4. *Mean concentration*

The mean concentration distribution can be computed using (3.17), (3.18) and (3.72) as

$$\langle C\rangle = C^{(0)} = \frac{1}{\sqrt{4\pi D_T t^*}} \exp\left(\frac{-\zeta^2}{4D_T t^*}\right). \tag{4.6}$$

https://doi.org/10.1017/jfm.2025.10691 Published online by Cambridge University Press

h	$Q=1$	$Q=5$	$Q=10$
0.0	0.008366	0.009160	0.011640
0.8	0.007524	0.007632	0.008098
1.0	0.006224	0.006109	0.006288

Table 3. Dispersion (D_T^*) values at various heights (h) for different pressure gradients (Q).

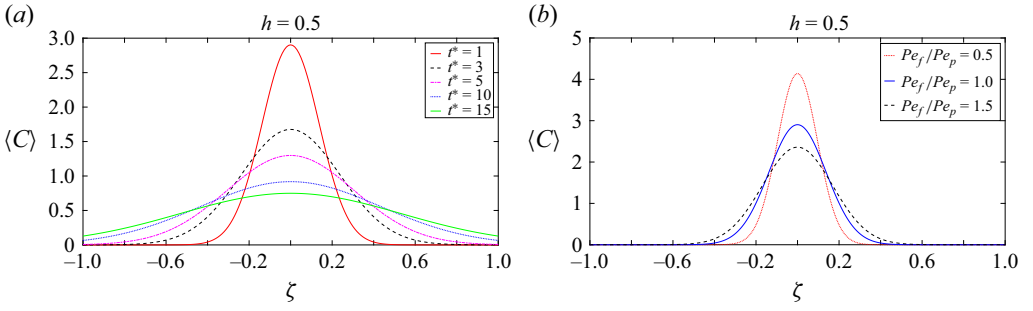


Figure 5. Longitudinal distribution of mean concentration distributions for different values of (a) time, where $M=1$, $Pe_p=Pe_f=1$, $Q=1$, $D_a=0.1$ and (b) Péclet numbers ratio, where $t^*=1$, $Q=1$, $M=1$, $D_a=0.1$.

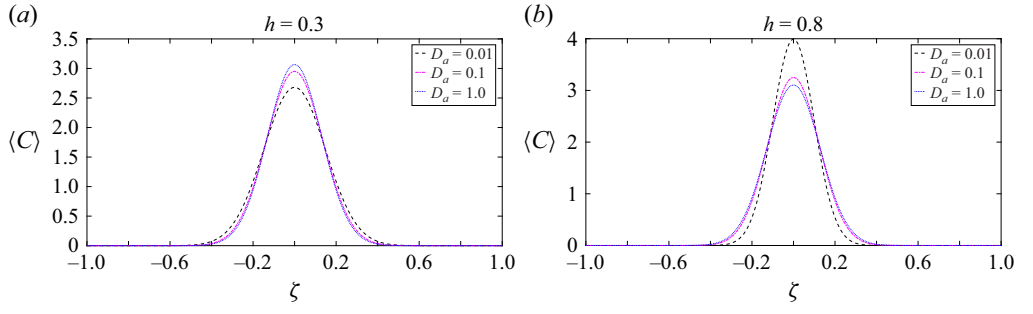


Figure 6. Longitudinal distribution of mean concentration distributions for $M=1$, $Pe_P=Pe_f=1$, $Q=1$ and $t^*=1$.

The variations of the longitudinal distribution of mean concentration can be seen from figures 5, 6 and 7. Figure 5(a) displays the change in the mean concentration distribution with time. At a fixed time, the mean concentration exhibits a Gaussian distribution, which is characterised by its symmetrical shape and adherence to statistical normality. The axis of symmetry remains unchanged, therefore partitioning the distribution into two symmetrical components. Over time, the apex of the distribution progressively decreases and becomes flatter.

The graph in figure 5(b) demonstrates how the ratio of the Péclet numbers (Pe_f/Pe_p) affects the mean concentration at a specific height ($h=0.5$). When (Pe_f/Pe_p) increases, the Péclet number of the fluid phase (Pe_f) becomes higher than that of the porous phase (Pe_p), resulting in a decrease in the peak of the mean concentration graph. This occurs because advection in the fluid phase becomes more influential, resulting into better transport of solutes. As a result, the solutes are more effectively carried away from the peak concentration point, causing a lower peak.

Figures 6(a) and 6(b) show that the mean concentration distribution undergoes significant changes with the Darcy number (D_a) in a two-layered channel flow. It is

https://doi.org/10.1017/jfm.2025.10691 Published online by Cambridge University Press

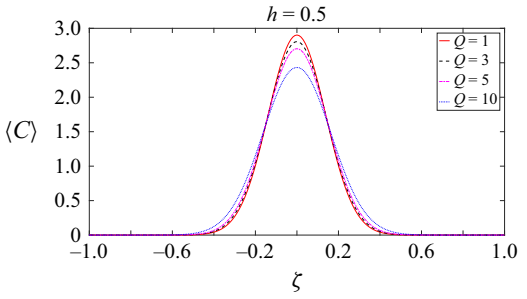


Figure 7. Longitudinal distribution of mean concentration distributions for $M = 1$, $Pe_p = Pe_f = 1$, $h = 0.5$, $D_a = 0.1$ and $t^* = 1$.

worth noting that these trends correlate with the behaviour of the dispersion coefficient, as demonstrated in figure 3. In figure 3(a) for $h = 0.3$, we can see that dispersion increases with a lower Darcy number, causing the peak of the mean concentration to decrease, as shown in figure 6(a). This happens because as D_a goes down, the effect of molecular diffusion on dispersion becomes stronger. This makes solutes spread out more and lowers their peak concentrations. Conversely, for $h = 0.8$, a lower D_a corresponds to decreased dispersion, resulting in an increased peak of the mean concentration, as illustrated in figure 6(b). In this case, advection is more prominent in the channel, carrying solutes away more quickly and thus reducing peak concentrations. Figure 7 displays the distribution of mean concentration for different Q values while keeping the parameters constant at $h = 0.5$. Our observation indicates that lower Q values result in a higher concentration peak, thus leading to greater solute spreading when the Q value is high. This finding is consistent with the dispersion graph presented in figure 4(b).

4.5. *Longitudinal concentration distribution*

The expression for the two-dimensional concentration distribution up to second order can be derived from (3.17) and (3.18) in the new coordinate system $\{\zeta, y\}$ as

$$C = \begin{cases} C^{(0)} + \epsilon Pe_p N_p(y) \dfrac{\partial C^{(0)}}{\partial \zeta} + \epsilon^2 Pe_p X_p(y) \dfrac{\partial^2 C^{(0)}}{\partial \zeta^2}, & 0 < y \leqslant h, \\ C^{(0)} + \epsilon Pe_f N_f(y) \dfrac{\partial C^{(0)}}{\partial \zeta} + \epsilon^2 Pe_f X_f(y) \dfrac{\partial^2 C^{(0)}}{\partial \zeta^2}, & h \leqslant y < 1. \end{cases} \tag{4.7}$$

Figures 8 and 9 show the longitudinal solute distribution along the channel, illustrating the gradual transition from zeroth order to second order at different times. Initially, for $t^* < 1$, the contributions of each order term are significant in shaping the solute concentration along the channel. However, as time progresses, the influence of higher-order terms diminishes. After $t^* = 1$, neglecting terms beyond the second order introduces minimal error, as indicated by figures 8 and 9. As a result, the graphs for zeroth-order, first-order and second-order approximations become nearly indistinguishable for a considerable period when $t^* > 1$.

Figures 10 and 11 display the concentration contours for different values of the parameters. Figure 10(a) presents the solute spreading dynamics over time in the two-layered channel system. Here, we plot the contour graphs for the porous region, which spans from 0 to 0.5 and the fluid region from 0.5 to 1. Initially, the solute is injected across the line $\zeta = 0$, the solute spreads due to advection and diffusion. The solute concentration experiences differential transport rates in the two regions: it travels faster in the fluid region compared with the porous area. This difference in transport velocities is primarily due to

https://doi.org/10.1017/jfm.2025.10691 Published online by Cambridge University Press

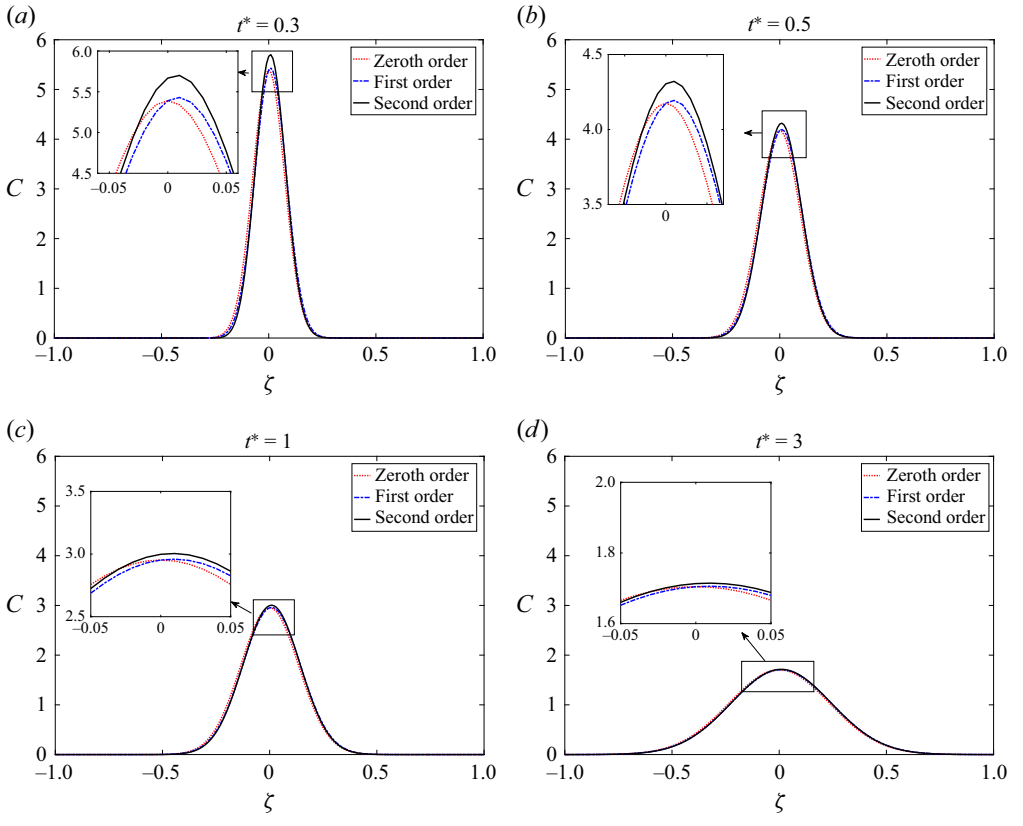


Figure 8. Longitudinal distribution of concentration calculated as asymptotic expansions from zeroth order to second order at different times, where $M = 1$, $Pe_p = Pe_f = 1$, $h = 0.3$, $Q = 1$, $y = 0.5$, $D_a = 0.1$.

the higher permeability and reduced resistance to flow in the fluid region, allowing solute molecules to move more freely. As time progresses, the concentration centroid experiences a reduction in its value, indicating the spreading of the solute throughout the channel. This phenomenon arises from advection, which propels solute downstream, and diffusion, which causes dispersion by random molecular motion, ultimately leading to a broader solute concentration distribution.

In figure 10(*b*) the observation of a ratio between two Péclet numbers (Pe_p/Pe_f) equals 0.5, resulting in the concentration cloud being at the origin near the bottom plate and near the upper plate along the y axis. As the ratio of these Péclet numbers increases, solute dispersion becomes more pronounced. Furthermore, the observation that the solute cloud spreads more in the fluid region than in the porous region suggests that the fluid layer is more efficient in transporting solutes over long distances due to higher advection effects. These trends align with the behaviour of the dispersion coefficient, which is influenced by the relative contributions of advection and diffusion in the two regions, impacting the overall spread of the solute cloud.

The observations in figures 11(*a*) and 11(*b*) provide valuable information into the behaviour of solute concentration distribution in a two-layered channel flow with differing heights ($h = 0.3$ and $h = 0.8$). In figure 11(*a*) at $h = 0.3$, it is clear that with decreasing Darcy number, solute spreads more. In contrast, at $h = 0.8$ (figure 11*b*), the opposite trend is observed, an increase in the Darcy number results in more solute spreading. These observations align with the behaviour of the dispersion coefficient, as a lower Darcy

https://doi.org/10.1017/jfm.2025.10691 Published online by Cambridge University Press

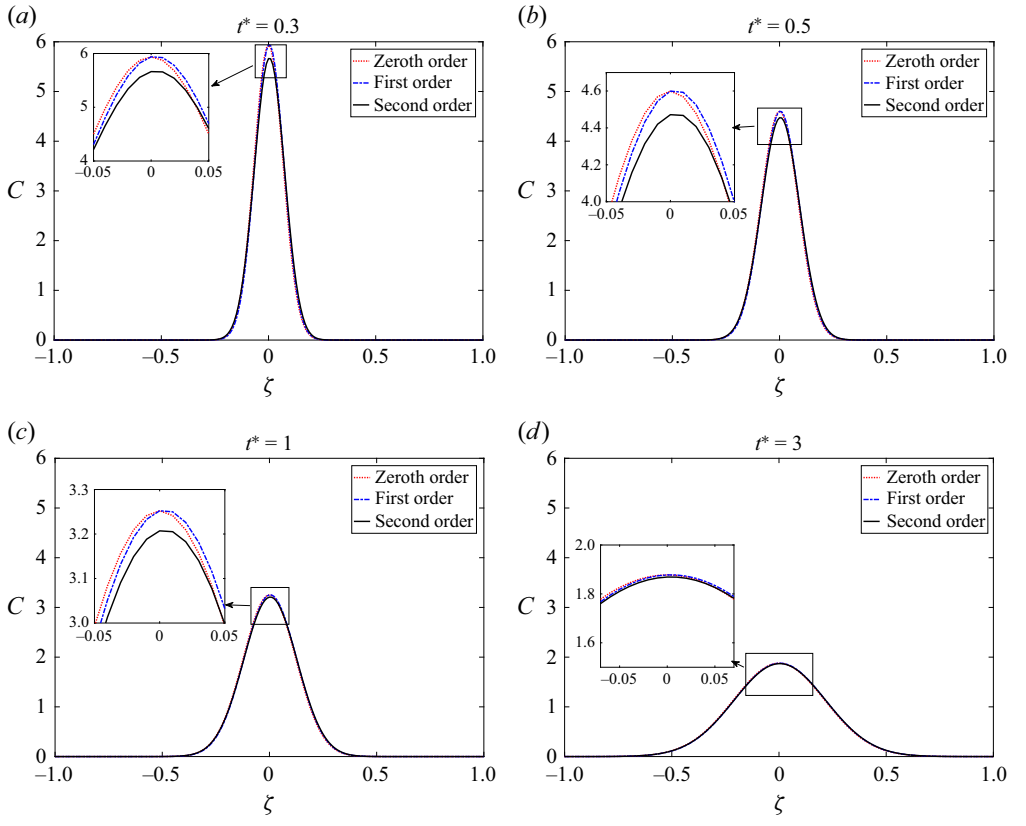


Figure 9. Longitudinal distribution of concentration calculated as asymptotic expansions from zeroth order to second order at different times, where $M = 1$, $Pe_p = Pe_f = 1$, $h = 0.8$, $Q = 1$, $y = 0.5$, $D_a = 0.1$.

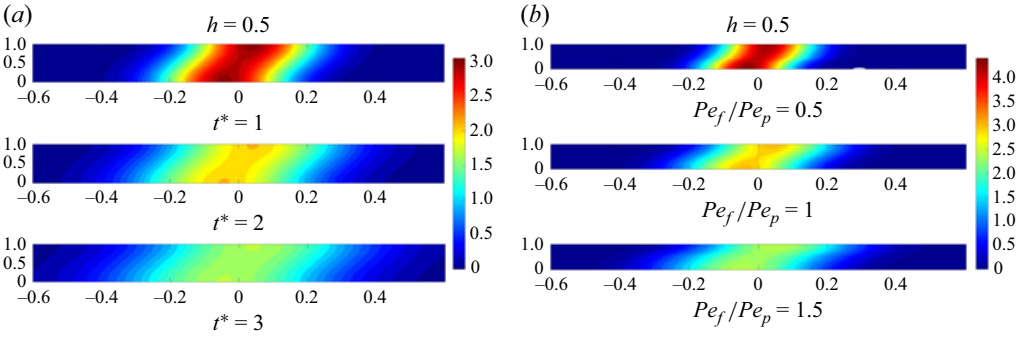


Figure 10. Concentration contour: the horizontal coordinate represents the variable ζ, while the vertical coordinate represents the variable y for different values of time (t^*) and Pe_f/Pe_p where (*a*) $M = 1$, $Q = 1$, $D_a = 0.1$, $Pe_p = Pe_f = 1$ and (*b*) $M = 1$, $D_a = 0.1$, $t^* = 1$, $Q = 1$.

number increases dispersion at $h = 0.3$, while a higher Darcy number does so at $h = 0.8$. The consistency between the dispersion and mean concentration results underline the interplay between advection and diffusion in influencing solute transport characteristics in two-layered channel flows with different heights.

https://doi.org/10.1017/jfm.2025.10691 Published online by Cambridge University Press

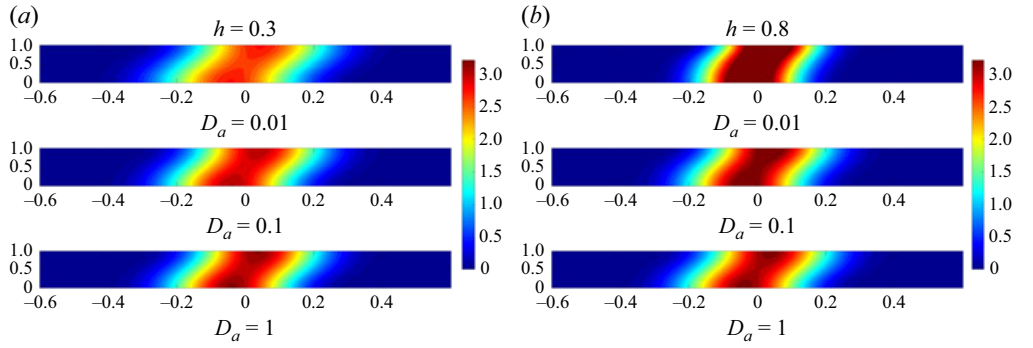


Figure 11. Concentration contours: the horizontal coordinate represents ζ, while the vertical coordinate represents y for different values of D_a where (*a*) $M = 1$, $Q = 1$, $Pe_p = Pe_f = 1$, $h = 0.3$ and (*b*) $M = 1$, $Q = 1$, $Pe_p = Pe_f = 1$, $h = 0.8$.

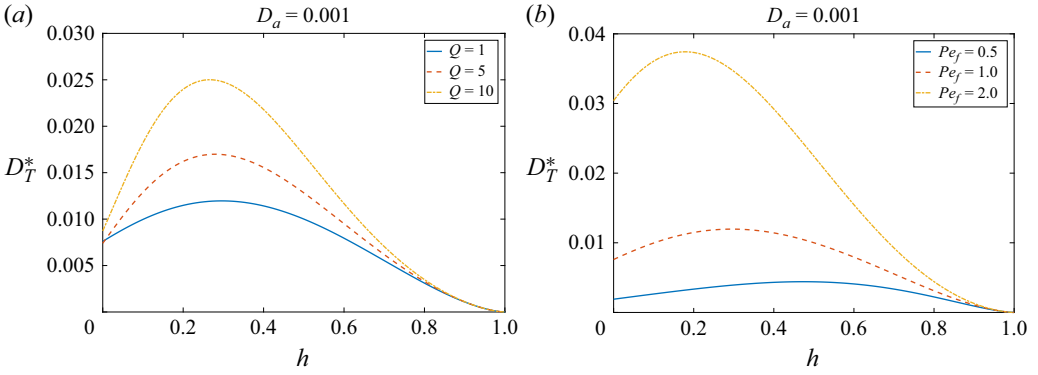


Figure 12. Dispersion graph of porous media using Darcy's law for (*a*) different Q and (*b*) different Pe_f.

4.6. *Application of classical Darcy model in porous region*

So far we were carrying out our investigations based on the extended Darcy equation (for the flow in porous media). However, based on one of the reviewers' suggestions, we have now carried out the studies based on pure Darcy equations for the flow with low Darcy numbers and the extended Darcy equation for the flows with greater than those Darcy numbers. Fluid flow through porous media has been characterised using the empirical relationship known as Darcy's law, i.e.

$$-\frac{\mathrm{d}p}{\mathrm{d}x'} - \mu\frac{u_p'(y')}{\kappa} = 0, \quad 0 \leqslant y' \leqslant h', \tag{4.8}$$

and the fluid motion in the fluid region (which is the same as (2.2))

$$-\frac{\mathrm{d}p}{\mathrm{d}x'} + \mu\frac{\mathrm{d}^2u_f'}{\mathrm{d}y'^2} = 0, \quad h' \leqslant y' \leqslant H. \tag{4.9}$$

The initial and boundary conditions are

$$u_p'(y') = u_b' \quad \text{at } y' = h', \tag{4.10}$$

$$\frac{\mathrm{d}u_f'(y')}{\mathrm{d}y'} = \beta'(u_b' - u_p') \quad \text{at } y' = h'. \tag{4.11}$$

https://doi.org/10.1017/jfm.2025.10691 Published online by Cambridge University Press

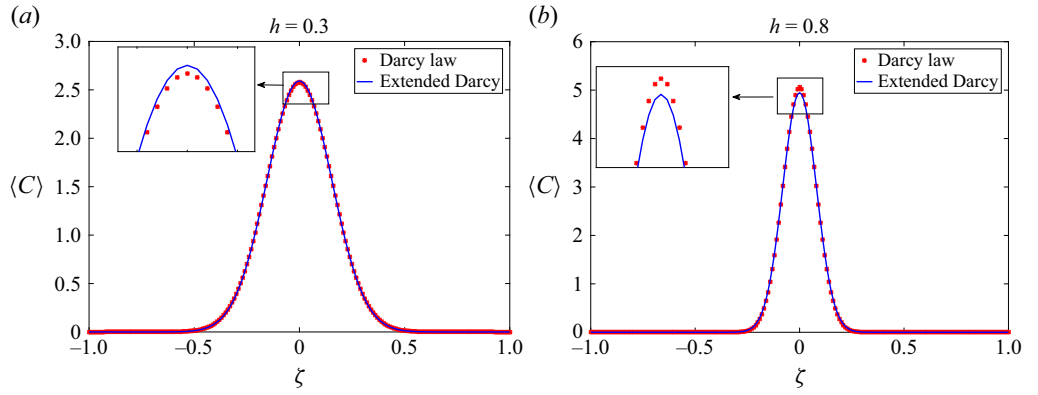


Figure 13. Longitudinal distribution of mean concentration distributions for different values of (*a*) $h = 0.3$, $t^* = 1$, $D_a = 0.001$, $Q = 1$, $M = 1$ and (*b*) $h = 0.8$, $t^* = 1$, $D_a = 0.001$, $Q = 1$, $M = 1$.

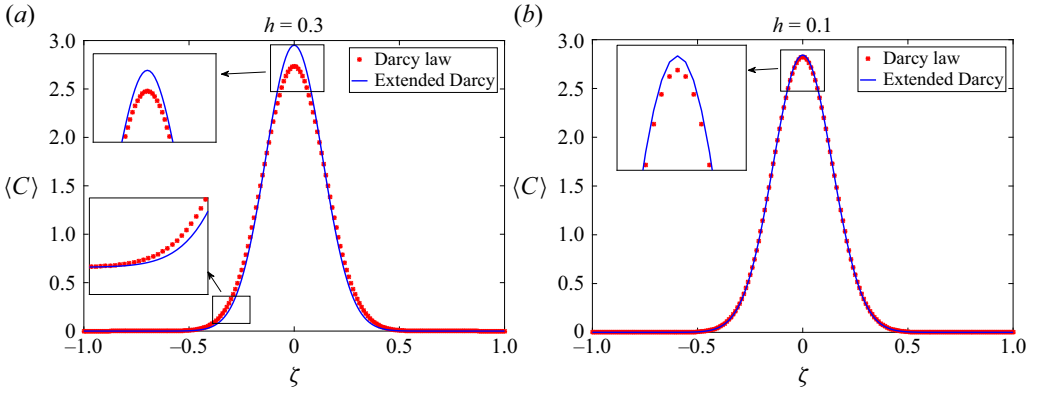


Figure 14. Longitudinal distribution of mean concentration distributions for different values of (*a*) $h = 0.3$, $t^* = 1$, $D_a = 0.1$, $Q = 1$, $M = 1$ and (*b*) $h = 0.1$, $t^* = 1$, $D_a = 0.001$, $Q = 1$, $M = 1$.

Here also U is the flow velocity of the free surface:

$$u_f'(y') = U \quad \text{at } y' = H. \tag{4.12}$$

Solving non-dimensional equations, we get the velocity components in the fluid and porous region, respectively, as

$$u_f = -Q\frac{y^2}{2} + (Qh + \beta(u_b - u_p))y + \left(1 + \frac{Q}{2} - Qh - \beta(u_b - u_p)\right), \tag{4.13}$$

$$u_p = QD_a, \tag{4.14}$$

$$u_b = \frac{Q\dfrac{h^2}{2} - Qh + 1 + \dfrac{Q}{2} - (h-1)\beta QD_a}{1 - (h-1)\beta}, \tag{4.15}$$

where u_b is the slip velocity and $\beta = (\alpha/\sqrt{\kappa})$ is a parameter that depends on permeable surface properties; α is a dimensionless parameter that contains structural characteristic of the porous media known as the slip coefficient, defined as $\alpha = \sqrt{(\mu/\mu_e)}$.

After obtaining the velocity profile, the multi-scale method is applied to determine the effective dispersion coefficient D_T^* and the mean concentration distribution $\langle C \rangle$. Figures 13 and 14 indicate that when the height (h) is small and permeability is low, the

https://doi.org/10.1017/jfm.2025.10691 Published online by Cambridge University Press

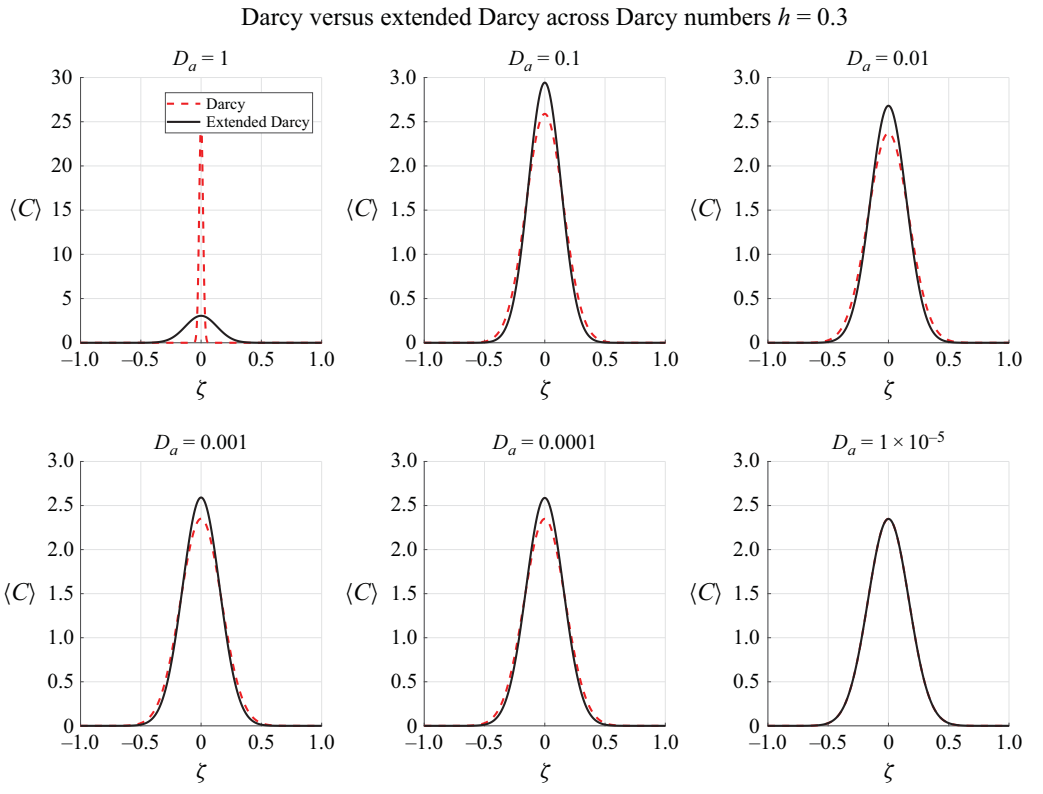


Figure 15. Darcy versus extended Darcy, where $h = 0.3$, $M = 1.05$, $Q = 1$, $t^* = 1$.

classical Darcy model and the extended Darcy model yield coinciding results. However, as (h) increases or permeability becomes significant, noticeable differences between the two models emerge. From this observation, we can conclude that in cases where the porous medium is very thin and exhibits high permeability, the classical Darcy model is appropriate. Conversely, in scenarios where the porous region is relatively thicker and the permeability is not significantly high, the extended Darcy model (Brinkman model) should be employed for more accurate predictions, supporting the results of Winter *et al.* (2022). We present a detailed comparison between the classical Darcy law and the extended Darcy (Brinkman) model by varying the channel thickness parameter h (considered at values $h = 0.3, 0.5, 0.8$) and the viscosity ratio M (taken as $M = 1$ and $M = 1.05$). For the case $M = 1$ with permeability $\kappa = 10^{-5}$, the difference between the Darcy and Brinkman models is not clearly visible (figure 13*b*). To highlight the distinction more effectively, we next consider the case $M = 1.05$ with $\kappa = 0.1$ (figure 15). For $D_a = 1$, the predictions of the extended Darcy (Brinkman) model differ markedly from the classical Darcy model, even for thin porous layers ($h = 0.3$). This is because the viscous penetration length is $\mathcal{O}(H)$, allowing interface shear to penetrate through the entire porous region. The classical Darcy model, lacking this shear-diffusion term, overconfines solute near the core. This aligns with studies showing that the Brinkman term becomes increasingly significant at higher permeability and across boundaries. For $D_a = 0.1$ and 0.01, the difference between the two models remains clear. The Brinkman solution continues to exhibit a smoother gradient at the interface and a broader profile. Here, the viscous penetration length ℓ_v is smaller but still larger than the porous thickness h, so shear penetration affects the

https://doi.org/10.1017/jfm.2025.10691 Published online by Cambridge University Press

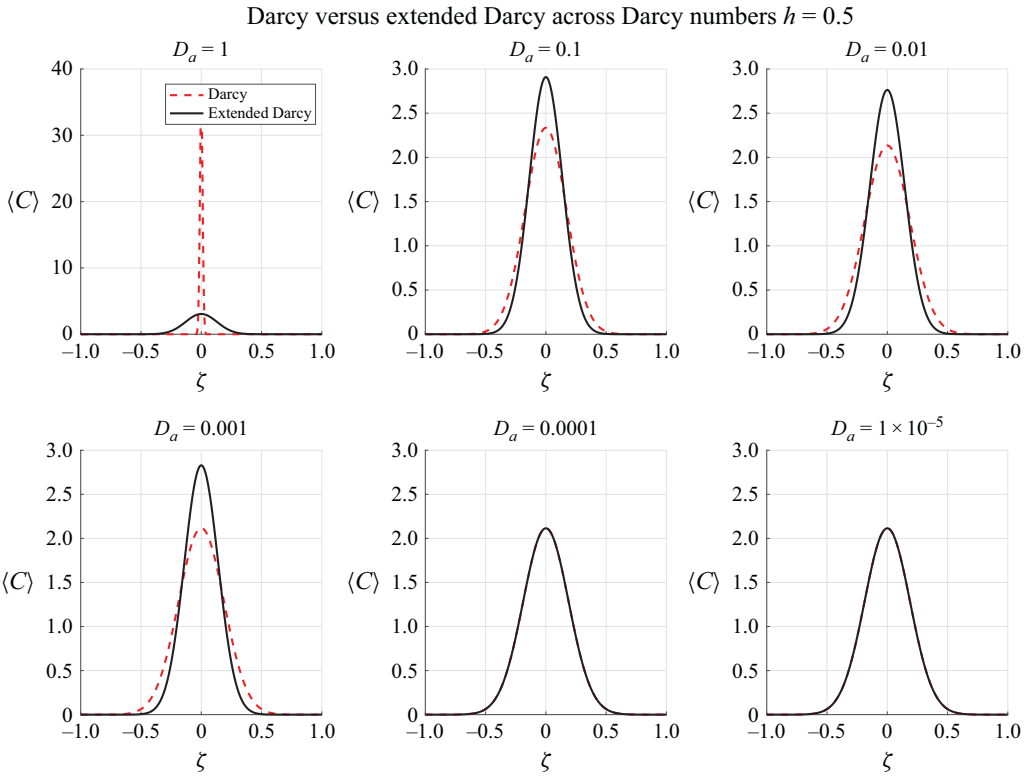


Figure 16. Darcy versus extended Darcy, where $h = 0.5$, $M = 1.05$, $Q = 1$, $t^* = 1$.

full porous layer. The Darcy model, lacking this mechanism, predicts a sharper decay of concentration towards the wall. When $D_a \leqslant 0.001$, permeability is low and the drag term dominates. In the Darcy model, the porous layer becomes nearly stagnant, and the concentration drops sharply near the wall. The extended Darcy model still shows slightly higher near-wall concentrations due to limited shear penetration, but because h is small the overall differences shrink compared with the high-D_a case.

In figures 16 and 17, when $D_a = 1$, the permeability κ is such that the viscous penetration length $\ell_v \sim \sqrt{\kappa}$ is of order H. This allows shear stresses from the free-fluid region to travel deep into the porous layer. The extended Darcy (Brinkman) model, which includes the $\mu_e \nabla^2 \boldsymbol{u}$ viscous diffusion term, transmits momentum into most of the porous thickness, sustaining a small but finite velocity there and enhancing cross-layer advection.The classical Darcy model neglects viscous shear inside the porous medium, producing a rapid velocity drop near the interface and confining solute transport largely to the free-fluid core. Because h is larger than in figure 15, the effect of Brinkman shear penetration is more pronounced, yielding broader $\langle C \rangle(\zeta)$ profiles and a lower centreline peak.

For $D_a = 0.1$ and 0.01, the viscous penetration length ℓ_v decreases but remains greater than h, allowing shear penetration to influence the entire porous layer. The Brinkman model still produces smoother gradients at the fluid–porous interface and broader concentration distributions than the Darcy model.

At low D_a, permeability is small and the drag term dominates. In the Darcy model the porous layer becomes nearly stagnant, resulting in a steep drop in concentration near the wall. The extended Darcy model still predicts slightly higher near-wall concentrations due

https://doi.org/10.1017/jfm.2025.10691 Published online by Cambridge University Press

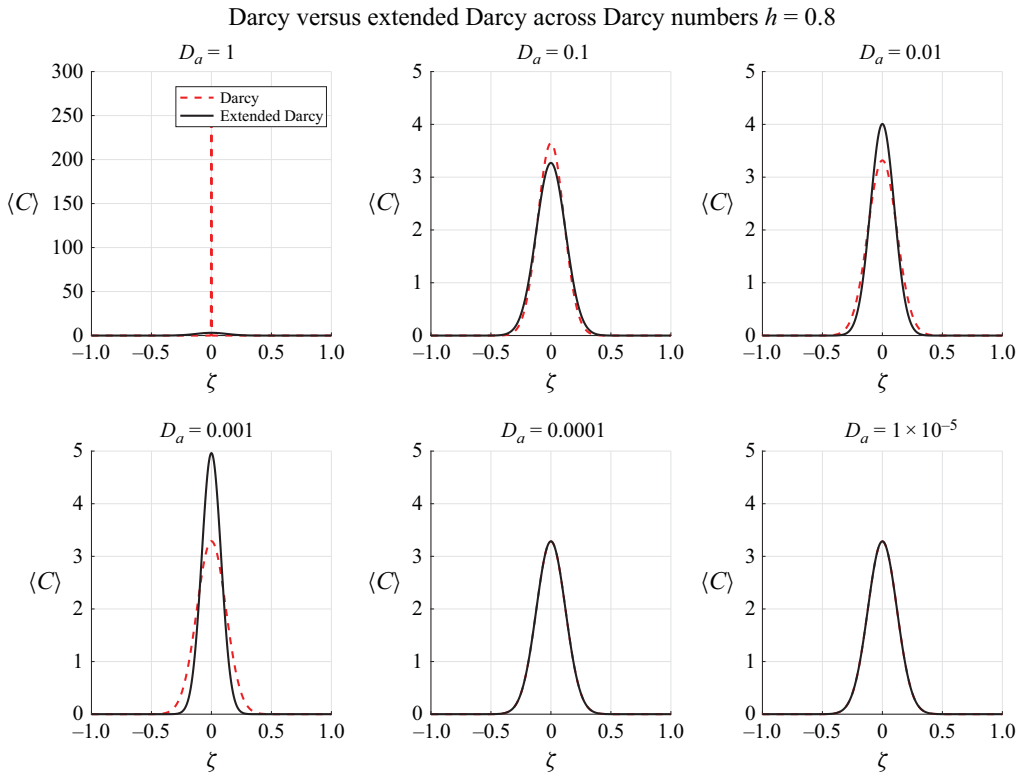


Figure 17. Darcy versus extended Darcy, where $h = 0.8$, $M = 1.05$, $Q = 1$, $t^* = 1$.

to limited shear penetration, but the differences are smaller than at high D_a. For $h = 0.5$, this weak advection effect remains more visible than in a thinner layer (figure 15).

Increasing h amplifies the impact of the Brinkman term at all Darcy numbers (figures 15, 16 and 17). For thick layers ($h = 0.8$), shear penetration influences a large volume of the porous medium, producing pronounced differences between the models across the entire D_a range. For moderate thickness ($h = 0.5$), the differences are still substantial at high D_a and remain visible at low D_a. Thin layers ($h = 0.3$) show the smallest – but still non-negligible – differences, particularly at high D_a where $\ell_v \gtrsim h$.

The extended Darcy (Brinkman) formulation is the physically consistent choice whenever (i) $D_a \gtrsim h^2$ or (ii) h is large enough for shear penetration to influence dispersion. The classical Darcy model is only adequate for thin layers with low permeability, where shear effects are negligible.

5. Conclusion

This comprehensive study investigates the intricate dynamics of a two-layered channel flow featuring dispersion in composite media within its layers. By formulating mass transport accurately, using fundamental momentum and solute transport equations adapted for two-layered channels, our research unveils critical implications for many applications. Mei's perturbation analysis for fluid dispersion in a single-layer channel has been extend for our insights in a two-zone channel flow, deriving an expression for concentration variation. Introducing distinct time scales for convection and diffusion processes, we consider the characteristic length and height of the channel, constructing two-time

https://doi.org/10.1017/jfm.2025.10691 Published online by Cambridge University Press

coordinates. Concentration has also been subjected to a similar two-scale expansion. The velocity profile for fully developed flow through a two-layered channel is derived as a specific case, revealing that velocity decreases as the height of the porous layer increases; moreover, an increase in Darcy number and pressure gradient results in an escalation of velocity. Dispersion dynamics is scrutinised, with dispersivity found to be contingent on the height of the porous region. As the Péclet number of fluid regions and the pressure gradient rises, dispersivity increases, while higher Darcy numbers yield flatter dispersivity trends. The mean concentration distribution is shown to impact the height of the porous region and decreases the peak of the concentration graph with an increase in pressure gradient. A two-dimensional concentration plot is presented, highlighting the effects of various parameters. A comparative analysis with results from a single-layer channel flow and the velocity profile for a specific case, along with dispersivity in a two-layer channel flow, reinforces the robustness of our findings. We also compared the analytical results with numerical solutions obtained using the finite difference method up to the second-order approximation, and found a close agreement between the two. In conclusion, our study provides a nuanced understanding of the multi-layered channel flow dynamics, offering valuable insights for diverse applications such as, for example, groundwater pollution. The meticulous comparison of our results with computational methods and existing literature underscores the significance and novelty of our contributions. We also determine the velocity profile, dispersion coefficient and mean concentration using the classical Darcy model for the porous region. The findings indicate that the classical Darcy model provides better accuracy compared with the extended Darcy model, especially in cases when the porous region is thin and has low permeability; in other cases the extended Darcy model is better suited.

Supplementary material. Supplementary material is available at https://doi.org/10.1017/jfm.2025.10691.

Acknowledgements. The authors extend their heartfelt gratitude to the referees for offering valuable suggestions to enhance the paper.

Funding. This research received no specific grant from any funding agency, commercial or not-for-profit sectors.

Declaration of interests. The authors report no conflict of interest.

Appendix A.

The complete mathematical expressions of I_1, I_2, $I_3(y)$, $I_4(y)$, I_5 to I_8, and, d_3 to d_{16}, as introduced in subsection (3.2), are presented as follows:

$$
\begin{aligned}
I_1 = &-\frac{1}{6}D_a Q(D_a Q - \langle u\rangle)\left(-h^3 + 6(D_a M)^{3/2}\sinh\left(\frac{h}{\sqrt{D_a M}}\right)\right)\\
&+\frac{1}{2}d_2\sqrt{D_a M}(D_a Q - \langle u\rangle)\left(-h^2 - 2D_a M + 2D_a M\cosh\left(\frac{h}{\sqrt{D_a M}}\right)\right)\\
&+d_3 D_a h Q - d_3 h\langle u\rangle - \frac{1}{6}D_a h^3 Q\langle u\rangle + \frac{h^3\langle u\rangle^2}{6}\\
&+\frac{1}{4}D_a^2 Q^2\left(2D_a h M + 4D_a h M\cosh\left(\frac{h}{\sqrt{D_a M}}\right)\right.\\
&\left.+2\sqrt{D_a M}\left(-h^2 - 2D_a M + D_a M\cosh\left(\frac{h}{\sqrt{D_a M}}\right)\right)\sinh\left(\frac{h}{\sqrt{D_a M}}\right)\right)\\
&-\frac{1}{2}D_a Q\left(-2d_2(D_a M)^{3/2} + 2D_a M(d_2\sqrt{D_a M} + h\langle u\rangle)\cosh\left(\frac{h}{\sqrt{D_a M}}\right)\right.
\end{aligned}
$$

https://doi.org/10.1017/jfm.2025.10691 Published online by Cambridge University Press

$$
\begin{aligned}
&- (2d_2 D_a h M + \sqrt{D_a M}(-2d_3 + h^2\langle u\rangle + 2D_a M\langle u\rangle)\sinh\left(\frac{h}{\sqrt{D_a M}}\right)\\
&+ d_2 (D_a M)^{3/2}\sinh\left(\frac{h}{\sqrt{D_a M}}\right)^2\Bigg)\\
&+\frac{1}{2}d_2 D_a Q\left(\sqrt{D_a M}(h^2+2D_a M)\cosh\left(\frac{h}{\sqrt{D_a M}}\right)\right.\\
&- (D_a M)^{3/2}\sinh\left(\frac{h}{\sqrt{D_a M}}\right)^2\\
&\left.- 2D_a M\left(\sqrt{D_a M} + h\sinh\left(\frac{h}{\sqrt{D_a M}}\right)\right)\right)\\
&+\frac{1}{4}d_2\left(-2d_2 D_a h M - 4d_3\sqrt{D_a M} + 4(D_a M)^{3/2}\langle u\rangle\right.\\
&- 2(2d_2 D_a h M + \sqrt{D_a M}(-2d_3 + h^2\langle u\rangle + 2D_a M\langle u\rangle))\cosh\left(\frac{h}{\sqrt{D_a M}}\right)\\
&+ 4D_a M(d_2\sqrt{D_a M} + h\langle u\rangle)\sinh\left(\frac{h}{\sqrt{D_a M}}\right)\\
&\left.+ d_2(D_a M)^{3/2}\sinh\left(\frac{2h}{\sqrt{D_a M}}\right)\right),
\end{aligned}
\tag{A1}
$$

$$
\begin{aligned}
I_2 = \frac{1}{5040}\Bigg[&-252d_1^2 - 132Q^2 - h\left(h\left(84d_1^2(-15+20h-10h^2+2h^3)\right.\right.\\
&+3(-140+70h+70h^2-49h^3+5h^5)Q^2\\
&-7d_1\left((-210+200h-15h^2-42h^3+15h^4)Q\right.\\
&\left.+60(9-8h+2h^2)(-1+\langle u\rangle)\right)\\
&+42(50-20h-15h^2+7h^3)Q(-1+\langle u\rangle)\\
&\left.+840(-3+h)(-1+\langle u\rangle)^2\right)\\
&+840d_4\left(6+3d_1(-2+h)-(-3+h^2)Q-6\langle u\rangle\right)\Bigg]\\
&+28d_1(45+13Q-45\langle u\rangle)\\
&+840d_4(6-3d_1+2Q-6\langle u\rangle)\\
&+924Q(-1+\langle u\rangle)-1680(-1+\langle u\rangle)^2,
\end{aligned}
\tag{A2}
$$

$$
\begin{aligned}
I_3(y) = &\frac{1}{2}Pe_p\left(\frac{1}{12}(D_a Q-\langle u\rangle)^2 y^4 - \frac{1}{3}d_2\sqrt{D_a M}(D_a Q-\langle u\rangle)y^3\right.\\
&-\frac{1}{2}\left(-MQ^2D_a^3 + d_2^2 M D_a - 2d_3 Q D_a + 2d_3\langle u\rangle\right)y^2\\
&-2D_a M\left(MQ^2D_a^3 - MQ\langle u\rangle D_a^2 - d_2^2 M D_a + d_2\sqrt{D_a M}Qy D_a\right.\\
&\left.\left.-d_2\sqrt{D_a M}\langle u\rangle y\right)\cosh\left(\frac{y}{\sqrt{D_a M}}\right)
\end{aligned}
$$

https://doi.org/10.1017/jfm.2025.10691 Published online by Cambridge University Press

$$
\begin{aligned}
&- D_a\sqrt{D_aM}\left(-2M\sqrt{D_aM}d_2^2 - 2M\langle u\rangle y d_2 + 6D_a^2M\sqrt{D_aM}Q^2\right.\\
&+ D_a\sqrt{D_aM}Q^2y^2 - \sqrt{D_aM}Q\langle u\rangle y^2 + 2d_3\sqrt{D_aM}Q\\
&\left.-6D_aM\sqrt{D_aM}Q\langle u\rangle\right)\cosh\left(\frac{y}{\sqrt{D_aM}}\right)\\
&+\frac{1}{4}D_a^2M^2\left(d_2^2 + D_a^2Q^2\right)\cosh\left(\frac{2y}{\sqrt{D_aM}}\right)\\
&- 2D_aM\sqrt{D_aM}\left(-D_a^2yQ^2 + D_a\langle u\rangle yQ + d_2\sqrt{D_aM}\langle u\rangle\right)\sinh\left(\frac{y}{\sqrt{D_aM}}\right)\\
&+ D_aM\left(-2\sqrt{D_aM}yd_2^2 + D_aQy^2d_2 - \langle u\rangle y^2d_2 + 2d_3d_2\right.\\
&+ 4D_a^2MQd_2 - 6D_aM\langle u\rangle d_2 + 2D_a^2\sqrt{D_aM}Q^2y\\
&\left.-2D_a\sqrt{D_aM}Q\langle u\rangle y\right)\sinh\left(\frac{y}{\sqrt{D_aM}}\right)\\
&-\frac{1}{2}d_2D_a^3M^2Q\sinh\left(\frac{2y}{\sqrt{D_aM}}\right)\Bigg),
\end{aligned}
\tag{A3}
$$

$$
\begin{aligned}
I_4(y) = &\frac{Pe_f}{5040}\left(\frac{15Q^2y^8}{8} - 15d_1Qy^7\right.\\
&+\frac{7}{2}\left(8d_1^2 + 14Qd_1 - 7Q(Q - 2\langle u\rangle + 2)\right)y^6\\
&+21\left(-8d_1^2 + (Q - 8\langle u\rangle + 8)d_1 + 2Q(Q - 3\langle u\rangle + 3)\right)y^5\\
&+\frac{35}{2}\left(24d_1^2 - 4(5Q - 12\langle u\rangle + 12)d_1\right.\\
&\left.+3\left(Q^2 - 4(d_4 + \langle u\rangle - 1)Q + 4(\langle u\rangle - 1)^2\right)\right)y^4\\
&-70\left(6d_1^2 - (12d_4 + 7Q - 18\langle u\rangle + 18)d_1\right.\\
&\left.+2\left(Q^2 - 5(\langle u\rangle - 1)Q + 6(\langle u\rangle - 1)^2\right)\right)y^3\\
&\left.+1260d_4(-2d_1 + Q - 2\langle u\rangle + 2)y^2\right),
\end{aligned}
\tag{A4}
$$

$$
\begin{aligned}
I_5 = &\frac{h}{Pe_p} - \frac{1}{Pe_p} - Pe_p\left(\frac{h^3\langle u\rangle^2}{6} - d_2d_3\sqrt{D_aM} + \frac{D_a^2Q^2h^3}{6} - d_3h\langle u\rangle - \frac{D_aMd_2^2h}{2}\right.\\
&-\frac{D_aQh^3\langle u\rangle}{3} + \frac{d_2h^2\langle u\rangle\sqrt{D_aM}}{2} + \frac{D_a^3MQ^2h}{2} + D_aQd_3h + d_2d_3\cosh\left(\frac{h}{\sqrt{D_aM}}\right)\sqrt{D_aM}\\
&+2D_aMd_2\langle u\rangle\sqrt{D_aM} - D_aQd_3\sinh\left(\frac{h}{\sqrt{D_aM}}\right)\sqrt{D_aM} - \frac{D_a^2MQd_2\sqrt{D_aM}}{2}\\
&\left.-\frac{D_a^2Q^2h^2\sinh\left(\frac{h}{\sqrt{D_aM}}\right)\sqrt{D_aM}}{2} - \frac{D_aQd_2h^2\sqrt{D_aM}}{2} + D_aMd_2^2\sinh\left(\frac{h}{\sqrt{D_aM}}\right)\sqrt{D_aM}\right.
\end{aligned}
$$

https://doi.org/10.1017/jfm.2025.10691 Published online by Cambridge University Press

$$+\frac{D_aMd_2^2\sinh\left(\frac{2h}{\sqrt{D_aM}}\right)\sqrt{D_aM}}{4}-D_aMd_2^2h\cosh\left(\frac{h}{\sqrt{D_aM}}\right)$$
$$-\frac{d_2h^2\langle u\rangle\cosh\left(\frac{h}{\sqrt{D_aM}}\right)\sqrt{D_aM}}{2}-2D_a^3MQ^2\sinh\left(\frac{h}{\sqrt{D_aM}}\right)\sqrt{D_aM}$$
$$+\frac{D_a^3MQ^2\sinh\left(\frac{2h}{\sqrt{D_aM}}\right)\sqrt{D_aM}}{4}+D_a^3MQ^2h\cosh\left(\frac{h}{\sqrt{D_aM}}\right)$$
$$+\frac{D_aQh^2\langle u\rangle\sinh\left(\frac{h}{\sqrt{D_aM}}\right)\sqrt{D_aM}}{2}-2D_aMd_2\langle u\rangle\cosh\left(\frac{h}{\sqrt{D_aM}}\right)\sqrt{D_aM}$$
$$+D_aMd_2h\langle u\rangle\sinh\left(\frac{h}{\sqrt{D_aM}}\right)+D_a^2MQd_2\cosh\left(\frac{h}{\sqrt{D_aM}}\right)\sqrt{D_aM}$$
$$-\frac{D_a^2MQd_2\cosh\left(\frac{2h}{\sqrt{D_aM}}\right)\sqrt{D_aM}}{2}+\frac{D_aQd_2h^2\cosh\left(\frac{h}{\sqrt{D_aM}}\right)\sqrt{D_aM}}{2}$$
$$+2D_a^2MQ\langle u\rangle\sinh\left(\frac{h}{\sqrt{D_aM}}\right)\sqrt{D_aM}-D_a^2MQh\langle u\rangle\cosh\left(\frac{h}{\sqrt{D_aM}}\right)\Bigg)$$
$$-\frac{h-1}{Pe_f}+Pe_f\left(\frac{11Q}{60}-\frac{d_1}{4}-d_4-\frac{2\langle u\rangle}{3}-\frac{13Qd_1}{180}-\frac{Qd_4}{3}\right.$$
$$-\frac{11Q\langle u\rangle}{60}+\frac{d_1d_4}{2}+d_4h+\frac{d_1\langle u\rangle}{4}+d_4\langle u\rangle-\frac{5Qh^2}{12}$$
$$+\frac{Qh^3}{6}+\frac{Qh^4}{8}-\frac{7Qh^5}{120}+\frac{3d_1h^2}{4}-\frac{2d_1h^3}{3}+\frac{d_1h^4}{6}+h^2\langle u\rangle$$
$$-\frac{h^3\langle u\rangle}{3}+\frac{11Q^2}{420}+\frac{d_1^2}{20}-\frac{h^2}{2}+\frac{h^3}{6}+\frac{\langle u\rangle^2}{3}-\frac{Q^2h^2}{12}$$
$$+\frac{Q^2h^3}{24}+\frac{Q^2h^4}{24}-\frac{7Q^2h^5}{240}+\frac{Q^2h^7}{336}-\frac{d_1^2h^2}{4}+\frac{d_1^2h^3}{3}$$
$$-\frac{d_1^2h^4}{6}+\frac{d_1^2h^5}{30}-\frac{h^2\langle u\rangle^2}{2}+\frac{h^3\langle u\rangle^2}{6}-\frac{3d_1h^2\langle u\rangle}{4}+\frac{2d_1h^3\langle u\rangle}{3}$$
$$-\frac{d_1h^4\langle u\rangle}{6}+\frac{Qd_4h}{2}-d_1d_4h-d_4h\langle u\rangle+\frac{7Qd_1h^2}{24}-\frac{5Qd_1h^3}{18}$$
$$+\frac{Qd_1h^4}{48}+\frac{7Qd_1h^5}{120}-\frac{Qd_1h^6}{48}-\frac{Qd_4h^3}{6}+\frac{5Qh^2\langle u\rangle}{12}-\frac{Qh^3\langle u\rangle}{6}$$
$$\left.-\frac{Qh^4\langle u\rangle}{8}+\frac{7Qh^5\langle u\rangle}{120}+\frac{d_1d_4h^2}{2}+\frac{1}{3}\right),\tag{A5}$$

$$I_6=\frac{h}{Pe_p}-\frac{1}{Pe_f}-Pe_p\left(\frac{h^3\langle u\rangle^2}{6}-d_2d_3\sqrt{D_aM}+\frac{D_a^2Q^2h^3}{6}-d_3h\langle u\rangle-\frac{D_aMd_2^2h}{2}\right.$$
$$\left.-\frac{D_aQh^3\langle u\rangle}{3}+\frac{d_2h^2\langle u\rangle\sqrt{D_aM}}{2}+\frac{D_a^3MQ^2h}{2}+D_aQd_3h+d_2d_3\cosh\left(\frac{h}{\sqrt{D_aM}}\right)\sqrt{D_aM}\right.$$

https://doi.org/10.1017/jfm.2025.10691 Published online by Cambridge University Press

$$+2D_aMd_2\langle u\rangle\sqrt{D_aM}-D_aQd_3\sinh\left(\frac{h}{\sqrt{D_aM}}\right)\sqrt{D_aM}-\frac{D_a^2MQd_2\sqrt{D_aM}}{2}$$
$$-\frac{D_a^2Q^2h^2\sinh\left(\frac{h}{\sqrt{D_aM}}\right)\sqrt{D_aM}}{2}-\frac{D_aQd_2h^2\sqrt{D_aM}}{2}+D_aMd_2^2\sinh\left(\frac{h}{\sqrt{D_aM}}\right)\sqrt{D_aM}$$
$$+\frac{D_aMd_2^2\sinh\left(\frac{2h}{\sqrt{D_aM}}\right)\sqrt{D_aM}}{4}-D_aMd_2^2h\cosh\left(\frac{h}{\sqrt{D_aM}}\right)$$
$$-\frac{d_2h^2\langle u\rangle\cosh\left(\frac{h}{\sqrt{D_aM}}\right)\sqrt{D_aM}}{2}-2D_a^3MQ^2\sinh\left(\frac{h}{\sqrt{D_aM}}\right)\sqrt{D_aM}$$
$$+\frac{D_a^3MQ^2\sinh\left(\frac{2h}{\sqrt{D_aM}}\right)\sqrt{D_aM}}{4}+D_a^3MQ^2h\cosh\left(\frac{h}{\sqrt{D_aM}}\right)$$
$$+\frac{D_aQh^2\langle u\rangle\sinh\left(\frac{h}{\sqrt{D_aM}}\right)\sqrt{D_aM}}{2}-2D_aMd_2\langle u\rangle\cosh\left(\frac{h}{\sqrt{D_aM}}\right)\sqrt{D_aM}$$
$$+D_aMd_2h\langle u\rangle\sinh\left(\frac{h}{\sqrt{D_aM}}\right)+D_a^2MQd_2\cosh\left(\frac{h}{\sqrt{D_aM}}\right)\sqrt{D_aM}$$
$$-\frac{D_a^2MQd_2\cosh\left(\frac{2h}{\sqrt{D_aM}}\right)\sqrt{D_aM}}{2}+\frac{D_aQd_2h^2\cosh\left(\frac{h}{\sqrt{D_aM}}\right)\sqrt{D_aM}}{2}$$
$$+2D_a^2MQ\langle u\rangle\sinh\left(\frac{h}{\sqrt{D_aM}}\right)\sqrt{D_aM}-D_a^2MQh\langle u\rangle\cosh\left(\frac{h}{\sqrt{D_aM}}\right)\Bigg)$$
$$-\frac{h-1}{Pe_f}+Pe_f\left(\frac{11Q}{60}-\frac{d_1}{4}-d_4-\frac{2\langle u\rangle}{3}-\frac{13Qd_1}{180}-\frac{Qd_4}{3}\right.$$
$$-\frac{11Q\langle u\rangle}{60}+\frac{d_1d_4}{2}+d_4h+\frac{d_1\langle u\rangle}{4}+d_4\langle u\rangle-\frac{5Qh^2}{12}$$
$$+\frac{Qh^3}{6}+\frac{Qh^4}{8}-\frac{7Qh^5}{120}+\frac{3d_1h^2}{4}-\frac{2d_1h^3}{3}+\frac{d_1h^4}{6}+h^2\langle u\rangle$$
$$-\frac{h^3\langle u\rangle}{3}+\frac{11Q^2}{420}+\frac{d_1^2}{20}-\frac{h^2}{2}+\frac{h^3}{6}+\frac{\langle u\rangle^2}{3}-\frac{Q^2h^2}{12}$$
$$+\frac{Q^2h^3}{24}+\frac{Q^2h^4}{24}-\frac{7Q^2h^5}{240}+\frac{Q^2h^7}{336}-\frac{d_1^2h^2}{4}+\frac{d_1^2h^3}{3}$$
$$-\frac{d_1^2h^4}{6}+\frac{d_1^2h^5}{30}-\frac{h^2\langle u\rangle^2}{2}+\frac{h^3\langle u\rangle^2}{6}-\frac{3d_1h^2\langle u\rangle}{4}+\frac{2d_1h^3\langle u\rangle}{3}$$
$$-\frac{d_1h^4\langle u\rangle}{6}+\frac{Qd_4h}{2}-d_1d_4h-d_4h\langle u\rangle+\frac{7Qd_1h^2}{24}-\frac{5Qd_1h^3}{18}$$
$$+\frac{Qd_1h^4}{48}+\frac{7Qd_1h^5}{120}-\frac{Qd_1h^6}{48}-\frac{Qd_4h^3}{6}+\frac{5Qh^2\langle u\rangle}{12}-\frac{Qh^3\langle u\rangle}{6}$$
$$\left.-\frac{Qh^4\langle u\rangle}{8}+\frac{7Qh^5\langle u\rangle}{120}+\frac{d_1d_4h^2}{2}+\frac{1}{3}\right), \tag{A6}$$

https://doi.org/10.1017/jfm.2025.10691 Published online by Cambridge University Press

$$I_7 = Pe_f \left(h \left(Pe_f \left(\frac{11Q}{60} - \frac{d_1}{4} - \frac{2\langle u\rangle}{3} - \frac{d_4\,(Q - 2d_1 - 2\langle u\rangle + 2)}{2} - \frac{13Qd_1}{180} + \frac{Qd_4}{6} \right.\right.\right.$$
$$- \frac{11Q\langle u\rangle}{60} - \frac{d_1 d_4}{2} + \frac{d_1\langle u\rangle}{4} + \frac{11Q^2}{420} + \frac{d_1^2}{20} + \frac{\langle u\rangle^2}{3} + \frac{1}{3} \Bigg) - \frac{h}{Pe_p} + \frac{1}{Pe_f} + Pe_p$$
$$\left(\frac{h^3\langle u\rangle^2}{6} - d_2 d_3 \sqrt{D_a M} + \frac{D_a^2 Q^2 h^3}{6} - d_3 h\langle u\rangle - \frac{D_a M d_2^2 h}{2} - \frac{D_a Q h^3\langle u\rangle}{3} \right.$$
$$+ \frac{d_2 h^2\langle u\rangle\sqrt{D_a M}}{2} + \frac{D_a^3 M Q^2 h}{2} + D_a Q d_3 h + d_2 d_3 \cosh\left(\frac{h}{\sqrt{D_a M}}\right)\sqrt{D_a M}$$
$$+ 2D_a M d_2\langle u\rangle\sqrt{D_a M} - D_a Q d_3 \sinh\left(\frac{h}{\sqrt{D_a M}}\right)\sqrt{D_a M} - \frac{D_a^2 M Q d_2\sqrt{D_a M}}{2}$$
$$- \frac{D_a^2 Q^2 h^2 \sinh\left(\frac{h}{\sqrt{D_a M}}\right)\sqrt{D_a M}}{2} - \frac{D_a Q d_2 h^2\sqrt{D_a M}}{2}$$
$$+ D_a M d_2^2 \sinh\left(\frac{h}{\sqrt{D_a M}}\right)\sqrt{D_a M} + \frac{D_a M d_2^2 \sinh\left(\frac{2h}{\sqrt{D_a M}}\right)\sqrt{D_a M}}{4}$$
$$- D_a M d_2^2 h \cosh\left(\frac{h}{\sqrt{D_a M}}\right) - \frac{d_2 h^2\langle u\rangle \cosh\left(\frac{h}{\sqrt{D_a M}}\right)\sqrt{D_a M}}{2}$$
$$- 2D_a^3 M Q^2 \sinh\left(\frac{h}{\sqrt{D_a M}}\right)\sqrt{D_a M} + \frac{D_a^3 M Q^2 \sinh\left(\frac{2h}{\sqrt{D_a M}}\right)\sqrt{D_a M}}{4}$$
$$+ D_a^3 M Q^2 h \cosh\left(\frac{h}{\sqrt{D_a M}}\right) + \frac{D_a Q h^2\langle u\rangle \sinh\left(\frac{h}{\sqrt{D_a M}}\right)\sqrt{D_a M}}{2}$$
$$- 2D_a M d_2\langle u\rangle \cosh\left(\frac{h}{\sqrt{D_a M}}\right)\sqrt{D_a M} + D_a M d_2 h\langle u\rangle \sinh\left(\frac{h}{\sqrt{D_a M}}\right)$$
$$+ D_a^2 M Q d_2 \cosh\left(\frac{h}{\sqrt{D_a M}}\right)\sqrt{D_a M} - \frac{D_a^2 M Q d_2 \cosh\left(\frac{2h}{\sqrt{D_a M}}\right)\sqrt{D_a M}}{2}$$
$$+ \frac{D_a Q d_2 h^2 \cosh\left(\frac{h}{\sqrt{D_a M}}\right)\sqrt{D_a M}}{2} + 2D_a^2 M Q\langle u\rangle \sinh\left(\frac{h}{\sqrt{D_a M}}\right)\sqrt{D_a M}$$
$$\left.\left.\left. - D_a^2 M Q h\langle u\rangle \cosh\left(\frac{h}{\sqrt{D_a M}}\right)\right)\right) - \frac{(h-1)}{Pe_f} - Pe_f \left(\frac{11Q}{60} - \frac{d_1}{4} - d_4 - \frac{2\langle u\rangle}{3} \right.$$
$$- \frac{13Qd_1}{180} - \frac{Qd_4}{3} - \frac{11Q\langle u\rangle}{60} + \frac{d_1 d_4}{2} + d_4 h + \frac{d_1\langle u\rangle}{4} + d_4\langle u\rangle - \frac{5Qh^2}{12} + \frac{Qh^3}{6}$$
$$+ \frac{Qh^4}{8} - \frac{7Qh^5}{120} + \frac{3d_1 h^2}{4} - \frac{2d_1 h^3}{3} + \frac{d_1 h^4}{6} + h^2\langle u\rangle - \frac{h^3\langle u\rangle}{3} + \frac{11Q^2}{420} + \frac{d_1^2}{20} - \frac{h^2}{2}$$
$$\left. + \frac{h^3}{6} + \frac{\langle u\rangle^2}{3} - \frac{Q^2 h^2}{12} + \frac{Q^2 h^3}{24} + \frac{Q^2 h^4}{24} - \frac{7Q^2 h^5}{240} + \frac{Q^2 h^7}{336} - \frac{d_1^2 h^2}{4} + \frac{d_1^2 h^3}{3} - \frac{d_1^2 h^4}{6} \right.$$

https://doi.org/10.1017/jfm.2025.10691 Published online by Cambridge University Press

$$+\frac{d_1^2h^5}{30}-\frac{h^2\langle u\rangle^2}{2}+\frac{h^3\langle u\rangle^2}{6}-\frac{3d_1h^2\langle u\rangle}{4}+\frac{2d_1h^3\langle u\rangle}{3}-\frac{d_1h^4\langle u\rangle}{6}+\frac{Qd_4h}{2}-d_1d_4h$$
$$-d_4h\langle u\rangle+\frac{7Qd_1h^2}{24}-\frac{5Qd_1h^3}{18}+\frac{Qd_1h^4}{48}+\frac{7Qd_1h^5}{120}-\frac{Qd_1h^6}{48}-\frac{Qd_4h^3}{6}$$
$$+\frac{5Qh^2\langle u\rangle}{12}-\frac{Qh^3\langle u\rangle}{6}-\frac{Qh^4\langle u\rangle}{8}+\frac{7Qh^5\langle u\rangle}{120}+\frac{d_4h^2\langle u\rangle}{3}-\frac{d_4h^3\langle u\rangle}{6}-\frac{h^4\langle u\rangle^2}{12}$$
$$+\frac{h^5\langle u\rangle^2}{60}-\frac{h^4d_1}{2}+\frac{h^5d_1}{3}-\frac{h^6d_1}{12}-\frac{h^5\langle u\rangle^2}{6}+\frac{h^6\langle u\rangle^2}{30}-\frac{d_1h^4\langle u\rangle^2}{6}+d_4h\langle u\rangle+\frac{d_4h^3}{6}$$
$$+\frac{h^2\langle u\rangle^2}{2}-\frac{d_4\langle u\rangle^2}{3}+\frac{d_4^2h^3}{6}-d_4^2h\langle u\rangle+\frac{d_4^2h^2\langle u\rangle}{2}-\frac{d_4^2h^4\langle u\rangle}{24}+d_4h^3\langle u\rangle+\frac{d_4h^4\langle u\rangle^2}{12}$$
$$+\frac{h^5}{60}-d_1h^3\langle u\rangle-\frac{d_1^2h^3}{12}+d_1^2h^2\langle u\rangle+d_1h^4\langle u\rangle-d_4h\langle u\rangle-\frac{d_4^2h^3\langle u\rangle^2}{12}-\frac{d_4h^2\langle u\rangle^2}{12}$$
$$+\frac{d_1^2d_4h^4}{12}+d_1d_4h^2+\frac{h^4\langle u\rangle^2}{12}-\frac{d_1d_4h^3\langle u\rangle^2}{12}-d_4h^2\langle u\rangle^2+d_4h^3\langle u\rangle+\frac{h^4d_1^2}{12}+\frac{h^5}{120} \tag{A7}$$

$$+\frac{d_1^2h^2\langle u\rangle^2}{6}+d_4^2h^3\langle u\rangle+d_4h^3\langle u\rangle+d_1h^4\langle u\rangle-d_1d_4h^4\langle u\rangle+d_1d_4h^4\langle u\rangle$$
$$+d_4^2h^3\langle u\rangle^2+\frac{d_1^2h^4\langle u\rangle^2}{12}-\frac{d_1d_4^2h^4\langle u\rangle^2}{12}+d_1d_4^2h^3\langle u\rangle+d_1^2d_4^2h^2\langle u\rangle^2+d_4^2h^4\langle u\rangle^2\Bigg)$$
$$-\frac{d_1d_4h^2}{2}+\frac{d_1^2h^2}{4}+\frac{d_1d_4h^3}{12}-\frac{d_4^2h^4}{12}+d_1^2h^2-d_1h^3+d_4h^4$$
$$+\frac{h^2d_1^2}{4}+d_1^2d_4h^2+\frac{h^2d_4^2}{12}+d_4^2h^4+d_4^2h^3, \tag{A8}$$

$$I_8=\frac{1}{336}\Bigg(-Q^2h^6+Q(Q-7d_1)h^5+\left(-\frac{44Q^2}{5}-\frac{98}{5}+\frac{63d_1}{5}+\frac{84\langle u\rangle}{5}\right)h^4$$
$$+\left(\frac{26Q^2}{5}+\frac{98d_1}{5}-\frac{126\langle u\langle}{5}+\frac{112}{5}\right)Qh^3$$
$$+\left(\frac{96Q^2}{5}+\frac{392}{5}-\frac{1106d_1}{15}-\frac{266\langle u\rangle}{5}-56d_4\right)Qh^2$$
$$+\left(-\frac{44Q^2}{5}-\frac{308}{5}-56d_4+\frac{154\langle u\rangle}{5}+\frac{364d_1}{15}\right)Qh-\frac{84d_1^2}{5}+84+168d_4-42\langle u\rangle$$
$$-\frac{44Q^2}{5}+\frac{364d_1}{15}+112d_4+\frac{154\langle u\rangle}{5}-\frac{308}{5}-\frac{84d_1^2}{5}+\Big(-168d_4-42\langle u\rangle+84\Big)d_1$$
$$-112+336d_4+112\langle u\rangle(h-1)\Bigg), \tag{A9}$$

$$d_3=\frac{1}{Pe_p}\{(1-h)(d_5Pe_p-d_6Pe_f)-(d_7Pe_p+d_8Pe_f)\}, \tag{A10}$$

$$d_4=-\frac{1}{Pe_f}\{h(d_5Pe_p-d_6Pe_f)+(d_7Pe_p+d_8Pe_f)\}, \tag{A11}$$

$$d_5=QDa\left\{-\frac{h^2}{2}+MDa\cosh\left(\frac{h}{\sqrt{MD_a}}\right)\right\}$$

https://doi.org/10.1017/jfm.2025.10691 Published online by Cambridge University Press

$$+ d_2\sqrt{MD_a}\left(h - \sqrt{MD_a}\sinh\left(\frac{h}{\sqrt{MD_a}}\right)\right) + \frac{\langle u\rangle}{2}h^2, \tag{A12}$$

$$d_6 = \left(h - \frac{h^2}{2}\right) - d_1\left(\frac{h}{2} - \frac{h^2}{2} + \frac{h^3}{6}\right) + \frac{Q}{2}\left(\frac{2h}{3} - \frac{h^2}{2} + \frac{h^4}{12}\right) - \langle u\rangle\left(h - \frac{h^2}{2}\right), \tag{A13}$$

$$d_7 = QDa\left(\frac{h^3}{6} - (MD_a)^{3/2}\sinh\left(\frac{h}{\sqrt{MD_a}}\right)\right) + d_2\sqrt{MDa}\left(MDa\cosh\left(\frac{h}{\sqrt{MD_a}}\right) - \frac{h^2}{2} - MDa\right) - \frac{\langle u\rangle}{6}h^3, \tag{A14}$$

$$d_8 = \left(-1 + \frac{d_1}{2} - \frac{Q}{3} + \langle u\rangle\right)\frac{1-h^2}{2} + \left(\frac{1}{2} - \frac{d_1}{2} + \frac{Q}{4} - \frac{\langle u\rangle}{2}\right)\frac{1-h^3}{3} + \frac{d_1}{24}\left(1-h^4\right) - \frac{Q}{120}\left(1-h^5\right), \tag{A15}$$

$$d_9 = -Pe_p\left(d_2\sqrt{D_aM}\left(MQD_a^2 - 2M\langle u\rangle D_a + d_3\right) - D_a^2MQd_2\sqrt{D_aM}\right), \tag{A16}$$

$$d_{10} = \frac{1}{Pe_p}\{d_{12}Pe_f + (d_{14} - d_{13})\}, \tag{A17}$$

$$d_{11} = -Pe_f\left(\frac{Q^2}{336} - \frac{d_1Q}{48} - \frac{\left(1 - d_1 + \frac{Q}{2}\right)Q}{120} + \frac{d_1^2}{30} - \frac{Q\left(\frac{1}{2} - \frac{d_1}{2} + \frac{Q}{4} - \frac{\langle u\rangle}{2}\right)}{10} + \frac{\left(1 - d_1 + \frac{Q}{2}\right)d_1}{24} + \frac{d_1\left(\frac{1}{2} - \frac{d_1}{2} + \frac{Q}{4} - \frac{\langle u\rangle}{2}\right)}{4} - \frac{Q\left(u - \frac{Q}{3} + \frac{d_1}{2} - 1\right)}{8} + \frac{\left(1 - d_1 + \frac{Q}{2}\right)\left(\frac{1}{2} - \frac{d_1}{2} + \frac{Q}{4} - \frac{\langle u\rangle}{2}\right)}{3} + \frac{d_1\left(\langle u\rangle - \frac{Q}{3} + \frac{d_1}{2} - 1\right)}{3} - \frac{Qd_4}{6} + \frac{\left(1 - d_1 + \frac{Q}{2}\right)\left(u - \frac{Q}{3} + \frac{d_1}{2} - 1\right)}{2} + \frac{d_1d_4}{2} + \left(1 - d_1 + \frac{Q}{2}\right)d_4\right) - I_6, \tag{A18}$$

$$d_{12} = \frac{1}{Pe_f}\left[h\left(d_{13} - d_{14}\right) - \left(d_{15} + d_{16}\right)\right], \tag{A19}$$

$$d_{13} = Pe_P\left(I_5h^2/2 + I_3|_{y=h} + d_9h\right), \tag{A20}$$

$$d_{14} = Pe_f\left(I_6h^2/2 + I_4|_{y=h} + d_{11}h\right), \tag{A21}$$

$$d_{15} = Pe_p\left(I_5\frac{h^3}{6} + I_7 + d_9\frac{h^2}{2}\right), \tag{A22}$$

$$d_{16} = Pe_f\left(I_6\frac{(1-h^3)}{6} + I_8 + \frac{d_{11}}{2}(1-h^2)\right). \tag{A23}$$

https://doi.org/10.1017/jfm.2025.10691 Published online by Cambridge University Press

Appendix B. Relationship between effective viscosity and slip model

Darcy's law provides a fundamental description of flow through the porous region under slow, steady and creeping flow conditions. It is written as

$$U = -\frac{\kappa}{\mu}\frac{\mathrm{d}p}{\mathrm{d}x}, \tag{B1}$$

where U is the Darcy velocity defined as the volumetric flow rate per unit total cross-sectional area (including both solid and fluid phases). Here, κ denotes the permeability of the medium, μ is the viscosity and $\mathrm{d}p/\mathrm{d}x$ is the pressure gradient.

However, within the pore space, the actual average velocity of the fluid, known as the interstitial velocity (u_{int}), is higher than the Darcy velocity and is defined as

$$u_{int} = \frac{U}{\phi}, \tag{B2}$$

where ϕ is the porosity, i.e. the fraction of the total volume occupied by voids. The distinction between U and u_{int} becomes critical in modelling near-interface behaviour because the free-fluid region interacts directly with the pore-level velocity field, not with the averaged Darcy velocity.

To model the fluid–porous interface, Beavers & Joseph (1967) introduced an empirical slip boundary condition, which relates the tangential shear rate in the fluid to the difference between the slip velocity in the fluid (u_s) and the interstitial velocity in the porous region (u_{int}), i.e.

$$\left.\frac{\mathrm{d}u}{\mathrm{d}y}\right|_{interface} = \frac{\alpha}{\sqrt{\kappa}}(u_s - u_{int}), \tag{B3}$$

where α is the slip coefficient.

To model this interface behaviour using a more mechanistic framework, the extended Darcy model is used. This model adds a viscous shear term to Darcy's law, resulting in

$$-\frac{\mathrm{d}p}{\mathrm{d}x} = \frac{\mu}{\kappa}u - \mu_e\frac{\mathrm{d}^2u}{\mathrm{d}y^2}, \tag{B4}$$

where μ_e is the effective viscosity in the porous region. It represents the resistance to tangential shear induced by the solid matrix of the porous medium. This term allows for a continuous velocity profile across the fluid–porous interface and models the smooth decay of velocity within the porous structure.

Solving (B4) in the porous region gives

$$u(y) = u_{int} + (u_s - u_{int})\exp\left(\frac{y}{\sqrt{\kappa}(\mu_e/\mu)}\right), \tag{B5}$$

subject to the following boundary conditions:

(i) $u(y \to -\infty) \to u_{int}$,
(ii) $u(y = 0) = u_s$.

From (B5), the shear rate at the interface is

$$\left.\frac{\mathrm{d}u}{\mathrm{d}y}\right|_{y=0} = \frac{\mu}{\sqrt{\kappa}\mu_e}(u_s - u_{int}). \tag{B6}$$

https://doi.org/10.1017/jfm.2025.10691 Published online by Cambridge University Press

Comparing (B6) with the Beavers–Joseph condition (B3), we obtain

$$\alpha = \sqrt{\frac{\mu}{\mu_e}}. \tag{B7}$$

This identity shows that the effective viscosity model and the slip model are physically and mathematically consistent. While the slip coefficient α is obtained from experiments, the extended Darcy model embeds this behaviour into the governing equations through μ_e, allowing a more systematic treatment in analytical and numerical modelling.

This equivalence also justifies the use of μ_e in the porous region as a mathematically robust and physically interpretable parameter to model near-interface velocity behaviour in layered systems.

Appendix C. Physical significance of effective viscosity in the Darcy–Brinkman equation

To accurately capture the momentum transport near porous–fluid interfaces, particularly in highly porous systems, the Darcy–Brinkman model introduces an effective viscosity, which extends the classical Darcy law by incorporating a viscous shear term. The effective viscosity arises in the modelling parameter of fluid flow through porous or composite media, especially in regions adjacent to interfaces between free fluid and porous layers. The effective viscosity value is not universal, it depends on the geometry, type of fluid, porosity, permeability of the medium and structure of the porous medium and often requires experimental and numerical (Hazra *et al.* 2004) fitting . In practical applications, μ_e is often treated as an adjustable fitting parameter to match experimental data or to ensure continuity of velocity and stress across interfaces. Although not physically measurable like true viscosity, it is widely accepted in engineering and computational modelling due to its ability to approximate realistic interfacial behaviour in complex porous systems. The term $\mu_e \nabla^2 u$ represents the viscous shear contribution in the Darcy–Brinkman equation and facilitates the imposition of a no-slip velocity condition on solid boundaries. Clearly when $u = 0$, the Darcy–Brinkman equation reduces to the Darcy equation.

C.1. *Effective viscosity μ_e versus viscosity μ*

Brinkman's original work suggested that μ_e could be approximated using Einstein's formula, i.e.

$$\frac{\mu_e}{\mu} \approx 1 + \frac{5}{2}(1 - \phi), \tag{C1}$$

where ϕ is the porosity. However, later theoretical and experimental studies demonstrated that μ_e may be higher or lower than μ depending on the pore structure. Koplik, Levine & Zee (1983) found that $\mu_e < \mu$ for low porosities, while Durlofsky & Brady (1987) and Martys et al. (1994) reported $\mu_e > \mu$ in more permeable media. Ochoa-Tapia & Whitaker (1995) suggested $\mu_e = \mu/\phi$, a simple empirical relation validated in several studies.

At interfaces between porous and clear fluid regions, μ_e is crucial for ensuring continuity of velocity and shear stress. If $\mu_e \neq \mu$, a stress jump condition may be required, which is proposed by Ochoa-Tapia & Whitaker (1995). Givler & Altobelli (1994) used Nuclear Magnetic Resonance to measure velocity profiles in open-cell foams with $\phi = 0.972$ and found $\mu_e \approx 7.5\mu$. Other studies have reported values from 0.5μ to 3μ, depending on the pore structure.

https://doi.org/10.1017/jfm.2025.10691 Published online by Cambridge University Press

Alazmi & Vafai (2001) found that variations in μ_e had minor effects on velocity and heat transfer in certain regimes, though they may be significant near interfaces.

We can conclude that the effective viscosity μ_e in the Darcy–Brinkman equation is essential for modelling shear effects in porous media and ensuring realistic interface behaviour. While often approximated as μ, its actual value depends on porosity and structure of the geometry and should be determined from theory or experiments when precision is required.

Appendix D. Two-dimensional transport model, including influence of two-dimensional advection

The general solutions of velocities of porous and fluid media are (which we previously obtained in (3.3)–(3.6))

$$u_p(y) = QD_a\left(1 - \cosh\left\{\frac{y}{\sqrt{MD_a}}\right\}\right) + d_2 \sinh\left\{\frac{y}{\sqrt{MD_a}}\right\} \tag{D1}$$

and

$$u_f(y) = 1 - d_1(1-y) + \frac{Q}{2}(1-y^2), \tag{D2}$$

where d_1 and d_2 are given as

$$d_1 = d_2\sqrt{\frac{M}{D_a}}\cosh\left\{\frac{1}{\sqrt{MD_a}}h\right\} - Q\sqrt{MD_a}\sinh\left\{\frac{1}{\sqrt{MD_a}}h\right\} + hQ, \tag{D3}$$

$$d_2 = \frac{1 + \frac{1}{2}Q(1-h)^2 - QD_a\left(1 - \cosh\left\{\frac{1}{\sqrt{MD_a}}h\right\}\right) + (1-h)Q\sqrt{MD_a}\sinh\left\{\frac{1}{\sqrt{MD_a}}h\right\}}{\sinh\left\{\frac{1}{\sqrt{MD_a}}h\right\} + \sqrt{\frac{M}{D_a}}(1-h)\cosh\left\{\frac{1}{\sqrt{MD_a}}h\right\}}. \tag{D4}$$

To find transverse velocity, we use equation of continuity,

$$\frac{\partial u}{\partial x} + \frac{\partial v}{\partial y} = 0. \tag{D5}$$

But in our case this is not possible, as using the equation of continuity, we get $v = 0$, which is obvious, as we assume fully developed flow, so for finding transverse velocity, let us assume very slight axial variation in u,

$$u(x, y) = u(y)(1 + \epsilon_1 x), \tag{D6}$$

where ϵ_1 is a parameter. Then we use the equation of continuity and we get the transverse velocity profiles for porous and fluid media:

$$v_p(y) = -\epsilon_1\left[y - d_1\left(y - \frac{y^2}{2} + \frac{Q}{2}\left(y - \frac{y^3}{3}\right)\right)\right], \tag{D7}$$

$$v_f(y) = -\epsilon_1\left[QD_a\left(y - \sqrt{MD_a}\sinh\left(\frac{y}{\sqrt{(MD_a)}}\right)\right) + d_2\sinh\left(\frac{y}{\sqrt{(MD_a)}}\right) + C_2\right]. \tag{D8}$$

Here

$$C_2 = 1 + \epsilon_1\left(QD_a\left(1 - \sqrt{MD_a}\sinh\left(\frac{1}{\sqrt{MD_a}} + d2\sqrt{MD_a}\cosh\left(\frac{1}{\sqrt{MD_a}}\right)\right)\right)\right). \tag{D9}$$

https://doi.org/10.1017/jfm.2025.10691 Published online by Cambridge University Press

After non-dimensionalisation in terms of space and time, the advection–diffusion equations and the associated initial and boundary conditions can be reformulated in terms of dimensionless space and time variables $\{\zeta, t^*\}$ as

$$Pe_p\langle\frac{1}{Pe}\rangle\frac{\partial C_p}{\partial t^*}+Pe_p(u_p-\langle u\rangle)\frac{\partial C_p}{\partial \zeta}+Pe_p v_p\frac{\partial C_p}{\partial y}=\frac{\partial^2 C_p}{\partial \zeta^2}+\frac{\partial^2 C_p}{\partial y^2},\quad 0<y\leqslant h, \tag{D10}$$

$$Pe_f\langle\frac{1}{Pe}\rangle\frac{\partial C_f}{\partial t^*}+Pe_f(u_f-\langle u\rangle)\frac{\partial C_f}{\partial \zeta}+Pe_f v_f\frac{\partial C_p}{\partial y}=\frac{\partial^2 C_f}{\partial \zeta^2}+\frac{\partial^2 C_f}{\partial y^2},\quad h\leqslant y<1, \tag{D11}$$

$$C_p(\zeta, y, t^*)\,|_{t^*=0}=\delta(\zeta),\quad 0<y\leqslant h, \tag{D12}$$

$$C_f(\zeta, y, t^*)\,|_{t^*=0}=\delta(\zeta),\quad h\leqslant y<1, \tag{D13}$$

$$\left.\frac{\partial C_p}{\partial y}\right|_{y=0}=\left.\frac{\partial C_f}{\partial y}\right|_{y=1}=0, \tag{D14}$$

$$C_p\,|_{y=h}=C_f\,|_{y=h}, \tag{D15}$$

and

$$\left.\frac{1}{Pe_p}\frac{\partial C_p}{\partial y}\right|_{y=h}=\left.\frac{1}{Pe_f}\frac{\partial C_f}{\partial y}\right|_{y=h}, \tag{D16}$$

$$C_p(\zeta, y, t^*)\,|_{\zeta\to\pm\infty}=0,\quad 0<y\leqslant h, \tag{D17}$$

$$C_f(\zeta, y, t^*)\,|_{\zeta\to\pm\infty}=0,\quad h\leqslant y<1. \tag{D18}$$

To validate the accuracy of the analytical solution, we performed a numerical simulation for the system of (D10)–(D18). The rectangular domain used for discretisation has dimensions of 40 units in length and 1 unit in width, with the length spanning from –20 to 20 and the width ranging from 0 to 1. The unsteady terms in (D10) and (D11) are discretised using a first-order forward difference scheme, while the advection term is approximated with a first-order upwind scheme. For the axial and transverse diffusion terms, we applied a second-order central difference scheme to discretise the second derivatives. Since v_p is not too large and accuracy is important, we use central difference. The resulting discretised governing equations, excluding the truncation error term, are given as

$$\begin{aligned}
&Pe_p\left\langle\frac{1}{Pe}\right\rangle\frac{C^{n+1}_{p_{i,j}}-C^{n}_{p_{i,j}}}{\Delta t^*}\\
&\quad+Pe_p\left\{\max(u_p-\langle u\rangle,0)\frac{C^{n}_{p_{i,j}}-C^{n}_{p_{i-1,j}}}{\Delta\zeta}-\max(\langle u\rangle-u_p,0)\frac{C^{n}_{p_{i+1,j}}-C^{n}_{p_{i,j}}}{\Delta\zeta}\right\}\\
&\quad+v_p(i,j)\frac{C^{n}_{p_{i,j+1}}-C^{n}_{p_{i-1,j}}}{2\Delta y}\\
&\quad=\frac{C^{n}_{p_{i+1,j}}-C^{n}_{p_{i-1,j}}}{\Delta\zeta^2}+\frac{C^{n}_{p_{i,j+1}}-2C^{n}_{p_{i,j}}+C^{n}_{p_{i,j-1}}}{\Delta y^2},\quad j=0,1,2,\ldots j_h,
\end{aligned} \tag{D19}$$

$$\begin{aligned}
&Pe_f\left\langle\frac{1}{Pe}\right\rangle\frac{C^{n+1}_{f_{i,j}}-C^{n}_{f_{i,j}}}{\Delta t^*}\\
&\quad+Pe_f\left\{\max(u_p-\langle u\rangle,0)\frac{C^{n}_{f_{i,j}}-C^{n}_{f_{i-1,j}}}{\Delta\zeta}-\max(\langle u\rangle-u_f,0)\frac{C^{n}_{f_{i+1,j}}-C^{n}_{f_{i,j}}}{\Delta\zeta}\right\}
\end{aligned}$$

https://doi.org/10.1017/jfm.2025.10691 Published online by Cambridge University Press

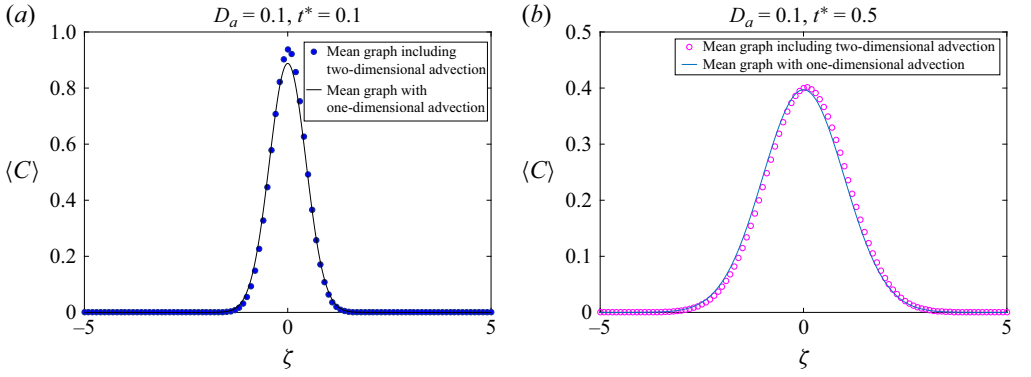


Figure 18. Comparison between the concentration profiles with and without transverse velocity at initial time (*a*) $t^* = 0.1$ and (*b*) $t^* = 0.5$.

$$+ v_f(i,\, j)\frac{C^n_{f_{i,j+1}} - C^n_{f_{i-1,j}}}{2\Delta y} = \frac{C^n_{f_{i+1,j}} - 2C^n_{f_{i,j}} + C^n_{f_{i-1,j}}}{\Delta\zeta^2} + \frac{C^n_{f_{i,j+1}} - 2C^n_{f_{i,j}} + C^n_{f_{i,j-1}}}{\Delta y^2}, \quad j = j_h, \ldots N_y. \tag{D20}$$

The boundary conditions in (D14) are discretised using three-point backward difference and forward difference schemes as

$$-3C_{p_{i,0}} + 4C_{p_{i,1}} - C_{p_{i,2}} = 0, \quad i = 0,\, 1,\, \ldots,\, M_x, \tag{D21}$$

and

$$3C_{f_{i,N_y}} - 4C_{f_{i,N_y-1}} + C_{p_{i,N_y-2}} = 0, \quad i = 0,\, 1,\, \ldots,\, M_x. \tag{D22}$$

The discretised expression for the boundary conditions (D17) and (D18) are as follows:

$$C_{p_{0,j}} = 0, \quad \textit{and} \quad C_{p_{M_x,j}} = 0, \quad j = 0,\, 1,\, \ldots,\, N_y, \tag{D23}$$

$$C_{f_{0,j}} = 0, \quad \textit{and} \quad C_{f_{M_x,j}} = 0, \quad j = 0,\, 1,\, \ldots,\, N_y. \tag{D24}$$

The discretised expression of the initial conditions (D12) and (D13) are given as

$$C_f = C_p = \begin{cases} 0 & 0 \leqslant i \leqslant M_x,\, 0 \leqslant j \leqslant N_y, \quad i \neq M_x/2, \\ 50 & i = M_x/2,\, 0 \leqslant j \leqslant N_y. \end{cases} \tag{D25}$$

The figures present a comparison between the numerically computed two-dimensional concentration profile with transverse velocity and without transverse velocity for solute transport in a two-layered system. Both plots correspond to a fixed Darcy number of 0.1. Figures 18(*a*) and 18(*b*) correspond to early time, the solute concentration exhibits a sharp and narrow peak near the centre of the domain. Figure 19 represents a later time, where the concentration profile becomes broader and the peak height decreases due to diffusion over time. For small D_a, there is a negligible difference that diminishes as time as well as Darcy number increases. The solution without transverse velocity closely matches the transverse velocity result, suggesting that the simplified model remains accurate even at later stages of the transport process.

https://doi.org/10.1017/jfm.2025.10691 Published online by Cambridge University Press

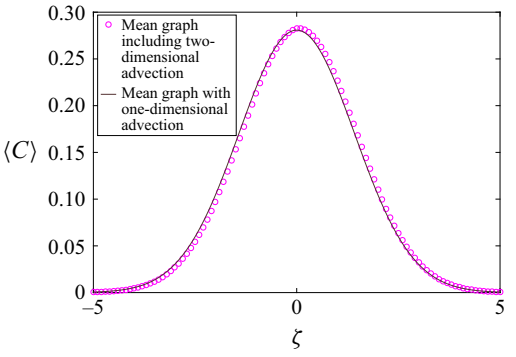


Figure 19. Comparison between the concentration profiles with and without transverse velocity at $t^* = 1$.

References

Alazmi, B. & Vafai, K. 2001 Analysis of fluid flow and heat transfer interfacial conditions between a porous medium and a fluid layer. *Intl J. Heat Mass Transfer* **44** (9), 1735–1749.

Aris, R.1956, On the dispersion of a solute in a fluid flowing through a tube. *Proc. R. Soc. Lond. A.* **235**(1200), 67–77.

Aris, R. 1960, On the dispersion of a solute in a pulsating flow through a tube. *Proc. R. Soc. Lond. A.* **259**(1298), 370–376.

Ault, J.T., Shin, S. & Stone, H.A. 2018 Diffusiophoresis in narrow channel flows. *J. Fluid Mech.* **854**, 420–448.

Barik, S. & Dalal, D.C. 2018 Transverse concentration distribution in an open channel flow with bed absorption: a multi-scale approach. *Commun. Nonlinear Sci.* **65**, 1–19.

Barik, S. & Dalal, D.C. 2019 Multi-scale analysis for concentration distribution in an oscillatory Couette flow. *Proc. Royal Soc. A* **475** (2221), 20180483.

Bear, J. 1961 On the tensor form of dispersion in porous media. *J. Geophys. Res.* **66** (4), 1185–1197.

Bear, J. 2013 *Dynamics of Fluids in Porous Media*. Courier Corporation.

Beavers, G.S. & Joseph, D.D. 1967 Boundary conditions at a naturally permeable wall. *J. Fluid Mech.* **30** (1), 197–207.

Brezinski, C. & Buffone, R. 1966 Dispersion in packed beds. *AIChE J.* **12** (5), 973–976.

Chen, G.Q. & Wu, Z.2012 Taylor dispersion in a two-zone packed tube. *Intl J. Heat Mass Transfer* **55** (1-3), 43–52.

Cvetkovic, V. & Dagan, G. 1994 Transport of kinetically sorbing solute by steady random velocity in heterogeneous porous formations. *J. Fluid Mech.* **265**, 189–215.

Cvetkovic, Vladimir, Dagan, G. & Cheng, H. 1998, Contaminant transport in aquifers with spatially variable hydraulic and sorption properties. *Proc. R. Soc. Lond. A.* **454** (1976), 2173–2207.

Das, D., Poddar, N., Dhar, S., Kairi, R.R. & Mondal, K.K. 2021 Multi-scale approach to analyze the dispersion of solute under the influence of homogeneous and inhomogeneous reactions through a channel. *Intl Commun. Heat Mass* **129**, 105709.

Dhar, S., Poddar, N., Mondal, K.K. & Mazumder, B.S. 2021 On dispersion of solute in a hydromagnetic flow between two parallel plates with boundary absorption. *Phys. Fluids* **33** (8), 083609.

Durlofsky, L. & Brady, J.F. 1987 Analysis of the Brinkman equation as a model for flow in porous media. *Phys. Fluids* **30** (11), 3329.

Fischer, H.B. 1973 Longitudinal dispersion and turbulent mixing in open-channel flow. *Annu. Rev. Fluid Mech.* **5** (1), 59–78.

Gill, W.N. & Sankarasubramanian, R.1970 Exact analysis of unsteady convective diffusion. *Proc. R. Soc. Lond. A.* **316**(1526), 341–350.

Gill, W.N., Sankarasubramanian, R. & Taylor, G.I. 1971 Dispersion of a non-uniform slug in time-dependent flow. *Proc. R. Soc. Lond. A.* **322**(1548), 101–117.

Givler, R.C. & Altobelli, E.S.A. 1994 A determination of the effective viscosity for the Brinkman–Forchheimer flow model. *J. Fluid Mech.* **258**, 355–370.

Hazra, S.B., Class, H., Helmig, R. & Schulz, V. 2004 Forward and inverse problems in modeling of multiphase flow and transport through porous media. *Computat. Geosci.* **8** (1), 21–47.

Hazra, S.B., Gupta, A.S. & Niyogi, P. 1996 On the dispersion of a solute in oscillating flow through a channel. *Heat Mass Transfer* **31** (4), 249–256.

https://doi.org/10.1017/jfm.2025.10691 Published online by Cambridge University Press

HAZRA, S.B., GUPTA, A. & NIYOGI, P. 1997 On the dispersion of a solute in oscillating flow of a non-Newtonian fluid in a channel. *Heat and Mass Transfer/Waerme- Und Stoffuebertragung* **32**, 481–488.

HINTON, E.M. & WOODS, A.W. 2019 The effect of vertically varying permeability on tracer dispersion. *J. Fluid Mech.* **860**, 384–407.

KOPLIK, J., LEVINE, H. & ZEE, A. 1983 Viscosity renormalization in the Brinkman equation. *Phys. Fluids* **26** (10), 2864–2870.

KUMAR, J.P., UMAVATHI, J.C., CHAMKHA, A.J. & BASAWARAJ, A. 2012 Solute dispersion between two parallel plates containing porous and fluid layers. *J. Porous Media* **15** (11).

KUZNETSOV, A.V. 1996 Analytical investigation of the fluid flow in the interface region between a porous medium and a clear fluid in channels partially filled with a porous medium. *Appl. Sci. Res.* **56**, 53–67.

KUZNETSOV, A.V. 1998 Analytical investigation of couette flow in a composite channel partially filled with a porous medium and partially with a clear fluid. *Intl J. Heat Mass Transfer* **41** (16), 2556–2560.

MARTYS, N., BENTZ, D.P. & GARBOCZI, E.J. 1994 Computer simulation study of the effective viscosity in Brinkman's equation. *Phys. Fluids* **6** (4), 1434–1439.

MAZUMDER, B.S. & DAS, S.K. 1992 Effect of boundary reaction on solute dispersion in pulsatile flow through a tube. *J. Fluid Mech.* **239**, 523–549.

MEI, C.C. 1992 Method of homogenization applied to dispersion in porous media. *Transport Porous Med.* **9**, 261–274.

MEI, C.C., AURIAULT, J.L. & NG, C.O. 1996 Some applications of the homogenization theory. *Adv. Appl. Mech.* **32**, 277–348.

MEI, C.C. & VERNESCU, B. 2010 *Homogenization Methods for Multiscale Mechanics*. World Scientific.

MILLINGTON, R.J. 1967 The dispersion of solute in a porous medium. *J. Fluid Mech.* **29** (3), 539–553.

NG, C.O. & MEI, C.C. 1996 Homogenization theory applied to soil vapor extraction in aggregated soils. *Phys. Fluids* **8** (9), 2298–2306.

NIELD, D.A., BEJAN, A. & 2006 *Convection in Porous Media*. vol. 3. Springer.

OCHOA-TAPIA, J.A. & WHITAKER, S. 1995 Momentum transfer at the boundary between a porous medium and a homogeneous fluid—II. Comparison with experiment. *Intl J. Heat Mass Transfer* **38** (14), 2647–2655.

PODDAR, N., DHAR, S., MAZUMDER, B.S. & MONDAL, K.K. 2021 An exact analysis of scalar transport in hydromagnetic flow between two parallel plates: a multi-scale approach. *Proc. Royal Soc. A* **477** (2248), 20200830.

POULIKAKOS, D. & KAZMIERCZAK, M. 1987 Forced convection in a duct partially filled with a porous material.

SAHU, C.K. & NEUFELD, J.A. 2020 Dispersive entrainment into gravity currents in porous media. *J. Fluid Mech.* **886**, A5.

SANKARASUBRAMANIAN, R. & W.N.GILL 1972 Dispersion from a prescribed concentration distribution in time variable flow. *Proc. R. Soc. Lond. A.* **329** (1579), 479–492.

SHIN, S., UM, E., SABASS, B., AULT, J.T., RAHIMI, M., WARREN, P.B. & STONE, H.A. 2016 Size-dependent control of colloid transport via solute gradients in dead-end channels. In *Proc. R. Soc. Lond. A.* vol 113, PP. 257–261.

TAYLOR, G. 1953 Dispersion of soluble matter in solvent flowing slowly though a tube. *Proc. R. Soc. London Ser. A* **219**, 186–203.

VAFAI, K. & KIM, S. 1990 Fluid mechanics of the interface region between a porous medium and a fluid layer—an exact solution. *Intl J. Heat Fluid Flow* **11** (3), 254–256.

VAFAI, K. & KIM, S.J. 1995 On the limitations of the Brinkman-Forchheimer-extended Darcy equation. *Intl J. Heat Fluid Flow* **16** (1), 11–15.

WANG, H., ZHU, Z., LI, S. & HUAI, W. 2019 Solute dispersion in wetland flows with bed absorption. *J. Hydrol.* **579**, 124149.

WINTER, R., VALSAMIDOU, A., CLASS, H. & FLEMISCH, B. 2022 A study on Darcy versus Forchheimer models for flow through heterogeneous landfills including macropores. *Water* **14** (4), 546.

WU, Z. & CHEN, G.Q. 2014 Approach to transverse uniformity of concentration distribution of a solute in a solvent flowing along a straight pipe. *J. Fluid Mech.* **740**, 196–213.

https://doi.org/10.1017/jfm.2025.10691 Published online by Cambridge University Press